Solid Earth Discuss., 3, 477–526, 2011
www.solid-earth-discuss.net/3/477/2011/
doi:10.5194/sed-3-477-2011

Solid Earth Discussions

Metamorphic history and geodynamic significance of the Early Cretaceous Sabzevar granulites (Sabzevar structural zone, NE Iran)

M. Nasrabady[1], **F. Rossetti**[2], **T. Theye**[3], **and G. Vignaroli**[2]

[1]Department of Geology, Imam Khomeini International University, Qazvin, Iran
[2]Dipartimento di Scienze Geologiche, Università Roma Tre, Roma, Italy
[3]Institut für Mineralogie, Universität Stuttgart, Stuttgart, Germany

Received: 11 May 2011 – Accepted: 14 May 2011 – Published: 19 May 2011

Correspondence to: F. Rossetti (rossetti@uniroma3.it)

Published by Copernicus Publications on behalf of the European Geosciences Union.

Abstract

The Iranian ophiolites are part of the vast orogenic suture zones that mark the Alpine-Himalayan convergence zone. Few petrological and geochronological data are available from these ophiolitic domains, hampering a full assessment of the timing and regimes of subduction zone metamorphism and orogenic construction in the region. This paper describes texture, geochemistry and the pressure-temperature path of the Early Cretaceous granulites that occur within the Tertiary Sabzevar suture zone of NE Iran. The geochemical data set document that the granulites are remnants of a MORB-type oceanic crust and thus of a (Early Cretaceous ?) back-arc basin formed in the upper plate of the Neotethyan subduction and thus interpreted as portions of a dismembered dynamothermal sole formed during oceanic subduction. The metamorphic history of the granulites suggests an anticlockwise pressure-temperature loop, compatible with burial in a hot subduction zone followed by cooling during exhumation. This is interpreted as the evidence of a nascent subduction zone formed at the expenses of hot and hence young oceanic lithosphere. These data point to diachronous and independent tectonic evolutions of the different ophiolitic domains of central Iran, for which a growing heterogeneity in the timing of metamorphic equilibration and of pressure-temperature paths can be expected with further investigations.

1 Introduction

Ophiolitic suture zones are the remnants of the oceanic lithosphere consumed during orogenic construction and testify for oceanic closure during continental collision at termination of a classical Wilson cycle of plate tectonics (e.g., Wilson, 1966; Dewey and Bird, 1970; Cawood et al., 2009). The metamorphic record of the oceanic-derived units marking orogenic suture zones provides key elements to decipher modes and regimes of oceanic subduction and to constrain paleotectonic reconstructions at (paleo-)convergent margins (e.g. Scambelluri et al., 1995; Peacock, 1996; Faccenna

SED
3, 477–526, 2011

et al., 2001a; Hacker et al, 2003; Jolivet et al., 2003; Brown, 2006, 2010; Bebout et al., 2007; Agard et al., 2009). High-grade, granulite facies metamorphism is not commonly reported in modern (Phanerozoic) subduction zone settings, being dominated by the burial of oceanic plates into the deep mantle by cold subduction (Hacker et al., 2003; Peacock et al., 1994; Stern, 2002; Brown, 2010). In these contexts, formation environments of mafic high-pressure granulite suites in orogenic settings have been generally ascribed to two-end member processes: arc maturation, i.e. formation in consequence of magmatic loading at the mature arc stage (e.g., Garrido et al., 2006; Berger et al., 2009), or melting remnants of a former oceanic crust in high heat-flow oceanic subduction settings (Peacock et al., 1994; Liu et al., 1997; Garcia Casco et al., 2008). The correct interpretation of the granulite-facies metamorphism in ophiolitic sutures is thus critical to understand both processes and history of oceanic subduction at convergent plate margins.

In this paper, we present new geochemical and petrological data on the Early Cretaceous migmatitic mafic granulites found within the Tertiary Sabzevar ophiolitic suture zone of northeast Iran (Rossetti et al., 2010) (Fig. 1), and describe their pressure-temperature (*P-T*) history. These data are used to shed light on the *P-T* regimes associated during closure of the ephemeral oceanic basins formed in the upper-plate of the Neo-Tethyan subduction during the long-lasting Alpine convergence involving Eurasia and Arabia. Implications in terms of the regional geodynamics and orogenic complex evolution are also discussed.

2 Geological background

The remnants of the Tethyan oceanic realm running from the Mediterranean through East Europe, Middle East to Asia form the widest Tertiary orogenic suture zone in the Erth (Fig. 1a). These ophiolitic rocks record a polyphase and prolonged history of oceanic construction (the Paleozoic-Early Mesozoic Paleo-Tethys and the Mesozoic-Cenozoic Neo-Tethys oceanic realms) and consumption during a sequence

SED
3, 477–526, 2011

of Late Paleozoic to Cenozoic subduction/obduction/collision stages localized along the Eurasian active plate margin (e.g., Ricou, 1994; Besse et al., 1998; Dercourt et al., 2000; Stampfli and Borel, 2002; Golonka, 2004; Maheo et al., 2004; Agard et al., 2006; Zanchi et al., 2006; Bagheri and Stampfli, 2008). The Iranian ophiolites are an integrant part of this evolving scenario, with the Neotethyan remnants distributed to mark diachronous closures of various oceanic branches during the Alpine-Himalayan convergence history (Takin, 1972; Stocklin, 1974; Alavi-Tehrani, 1977; Sengör et al., 1988; McCall, 1997; Ghasemi and Talbot, 2006; Bagheri and Stampfli, 2008, and references therein).

The NW-SE trending ophiolitic belt of the Sabzevar Range is part of the Tertiary ophiolitic suture zones that surround the Central Iranian Microcontinent (CEIM; Figs. 1b and 2a). This ophiolitic domain is the remnant of one of the peri-Tethyan oceanic branches (referred as the Sabzevar Ocean; Sengör et al., 1988; Mc Call, 1997; Bagheri and Stampfli, 2008) that bordered the northern margin of the CEIM toward the Asian Turan plate (Fig. 1b). It constitutes the largest ophiolitic massif (150 km long and 10–30 km wide) of north-eastern Iran and consists of a dismembered ophiolitic suite, with a tectonised and extensively serpentinised mantle section (harzburgite, dunite and lherzolite) intruded by mafic magmas and a volcano-sedimentary sequence, Late Cretaceous to Paleocene in age (Alavi-Tehrani, 1977; Delaloye and Desmons, 1980; Baroz et al., 1984; Shojaat et al., 2003). The geochemical signature of the ophiolitic rocks attests for a general MORB-like signature, suggesting that the oceanic lithosphere developed at an oceanic spreading center (Baroz et al., 1984; Shojaat et al., 2003). These ophiolitic rocks dominantly occur dispersed as centimetre- to kilometre-size blocks into a highly sheared serpentinite matrix to form a major ophiolitic tectonic mélange. The blocks consist of serpentinised peridotites and intrusive and extrusive rocks, but foliated metabasites (blueschists, greenschists and amphibolites) are also present. Syn-to-late tectonic, variably sized granitic bodies intrude the ophiolitic mélange, postdating main fabric development in the ophiolitic mélange and inducing contact metamorphism in the host rocks (Baroz et al., 1984). Another mélange unit

SED
3, 477–526, 2011

underlies the tectonic mélange and consists of SE-verging imbricated thrust slices of red cherts and volcanic-volcaniclastic rocks, with characters peculiar of a subduction-accretion complex (e.g. von Huene and Scholl, 1991) and forming the frontal part of the range. The age of rock units and the timing of metamorphism in the orogenic pile of the Sabzevar Range have been constrained by K-Ar muscovite and Rb-Sr whole rock and micas geochronology. These data document that granitic magmatism occurred in the Early Eocene (at about 50 Ma), synchronous with the main greenschist-to-amphibolite retrograde metamorphism recorded in the metabasite blocks (Baroz et al., 1984)

Two exposures of km-scale, mafic granulite bodies were recognised within the serpentinite mélange exposed in the NW portion of Sabzevar Range, to the north of the Novdeh and to the south of the Zarghan villages, respectively (Fig. 2a). Structurally, the granulite bodies occur as tectonic slivers embedded within the surrounding sheared serpentinite mélange (Fig. 2b–c). The field relationships with the mélange are usually obscured by intense fracturing and faulting related to regional, post-orogenic strike-slip tectonics. The age of the granulite metamorphism was established through in situ U(-Th)-Pb zircon and titanite geochronology, which point to an Early Cretaceous age (ca. 105 Ma) (Rossetti et al., 2010). This age thus contrasts with the Late Cretaceous formation age of the Sabzevar ophiolites and imposes re-consideration of the current tectonic models for the Alpine convergence history of the region.

3 Granulite texture and petrography

The granulite bodies are dark, medium to fine-grained rocks showing granoblastic groundmass or weak foliation (Fig. 3a). Texture is dominated by the occurrence of millimetric-to-centimetric leucocratic patches and layers (leucosomes) interlayered within the mafic host rock mineral matrix (melanosome), giving the rock a migmatitic appearance (Fig. 3a–c). This study reports data on four granulite samples, selected from a representative regional sampling on the basis of (i) preservation of the granulite facies assemblage and lack of pervasive amphibolite retrogression (sample NG353

SED
3, 477–526, 2011

and NG421); and (ii) evidence of retrograde amphibolite replacement (samples SZ290, EG354D). In the following, mineral abbreviations follow Whitney and Evans (2010).

3.1 Host rock

The mafic host rock makes up the bulk (>90 %) of rocks and primarily define the main, coarse foliation in the outcrop and in the hand samples. The mineral assemblage mainly consists of amphibole + garnet + clinopyroxene with minor plagioclase ± quartz. Rutile, titanite, ilmenite, zircon and apatite occur as accessory minerals. The texture is granoblastic, with the exception of quartz and plagioclase that mostly occurs as interstitial, curvilinear grains. Quartz also occurs as rounded inclusions in coarser grained matrix amphibole, garnet and clinopyroxene. In samples NG353 and NG421, matrix garnets are medium-grained (1 to 5 mm) porphyroblasts and are usually poikiloblastic, hosting clinopyroxene (Cpx_1), amphibole (Amp_1), plagioclase (Pl_1), quartz, rutile, ilmenite, titanite, as inclusions (Figs. 3d–e and 4). In particular, amphibole $Amph_1$, Pl_1, $ilmenite_1$/$titanite_1$ and quartz form composite inclusions hosted at the garnet cores, whereas while Cpx_1 occurs in the rim regions (Fig. 4a–h). Particularly relevant for the metamorphic evolution of the Sabzevar granulites is the sequence in the Ti mineral phases with respect to garnet crystallisation and matrix assemblages. The earliest Ti mineral record, preserved in garnet, is represented by $titanite_1$, often preserved shielded in $ilmenite_1$ or in equilibrium with $ilmenite_1$ (Fig. 4b, d and g). Also mm-sized euhedral ilmenite-clinopyroxene-bearing pseudomorphs after titanite are often observed (Fig. 4d). The formation of $titanite_1$ predated the major garnet growth episode. This is also the case for a few single-phase $ilmenite_1$ inclusions in garnet and for the replacement of $titanite_1$ by $ilmenite_1$. Small single-phase rutile inclusions are abundant in garnet cores and rims (Fig. 4c and h). Accordingly, this mineral was stable during the main growth episode of garnet. As observed in some garnet grains, rutile crystallized at the expense of $ilmenite_1$ (Fig. 4c). In contrast, no rutile is present in the matrix. It exclusively survived as shielded inclusions in garnet or in some lager ilmenite grains. After or at the very end of the main garnet growth period, abundant $ilmenite_2$

SED
3, 477–526, 2011

crystallized in the matrix, partly directly at the expense of matrix rutile (Figs. 3d and 4i). Accordingly, the formation of Ti minerals can be temporarily grouped and related to major garnet growth: titanite$_1$ → ilmenite$_1$ → rutile → ilmenite$_2$. Both titanite$_1$ and ilmenite$_1$ predated garnet growth, rutile was stable during the major garnet growth period, and ilmenite$_2$ postdate garnet. A lately formed second generation of titanite occurs in the leucosome. In the heavily retrogressed samples, garnet is porphyroclastic, usually showing strong evidence for resorption with development of plagioclase + amphibole symplectites and final break-down to form chlorite-epidote-amphibole composite association (Fig. 3f).

Clinopyroxene is usually found as main constituent of the matrix assemblage (Cpx$_2$). It consists of medium-to-fine grained grains, seldom containing inclusions of ilmenite, plagioclase, quartz, and amphibole (Fig. 3d). Plagioclase is found as main constituent of the inclusion assemblage found in garnet and clinopyroxene (Pl$_1$), but also occur as small, interstitial grains in matrix assemblages (Pl$_2$) (Fig. 3d). Four textural varieties of amphibole are identified: (i) amphibole inclusions within garnet and clinopyroxene (Amp$_1$) (Figs. 3d and 4b, e); (ii) coarse-grained matrix grains (Amp$_2$), with clear equilibrium textural relationships with garnet and clinpyroxene (Figs. 3d and 4h); (iii) symplectite- and corona-type amphibole (Am$_3$) intergrown with plagioclase and quartz around garnet grains and clinopyroxene (Fig. 3e); and (iv) pale green amphibole (Amp$_4$) crystallised after garnet breakdown (Fig. 3f). Texturally-late veins also occur, dominantly consisting of prehnite and albite with minor chlorite and epidote (Fig. 3g). In the heavily retrogressed samples, epidote form pseudomorphous aggregates replacing garnet, while prehnite, albite and chlorite appear in the matrix.

3.2 Leucosome

The leucosomes invariably consist of plagioclase + quartz-rich continuous and concordant segregations of broadly tonalitic/trondhjemitic composition (modal proportions of quartz to plagioclase of 50–35/50–65). The leucosomes shows a systematic intragranular connectivity, with plagioclase and quartz showing a coarse granoblastic

SED
3, 477–526, 2011

texture (Rossetti et al., 2010). Large xenomorphic (1–2 mm) quartz grains also characterise many leucosomes, with these grains extending and dispersing outwards into the amphibole-rich host rock (Fig. 3h). Titanite (Ttn_2) is also found in the leucosomes and is usually inclusion free. Plagioclase + quartz associations also form film-like intergrowth surrounding matrix amphibole. Little evidence for solid-state deformation is documented, mostly attested by patchy undulose extinction in some quartz grains. In retrogressed samples, plagioclase is pseudomorphosed by prehnite-albite composite associations (Fig. 3h).

4 Whole rock geochemistry

Nine samples were geochemically analysed to constrain the tectonic setting on which their precursor rocks formed (Table 1). Major and trace element abundances were obtained by inductively coupled plasma mass spectrometry (ICP-MS) at Activation Labs in Canada (analysis protocol 4E Research; method described in Hoffman, 1992).

Major element analysis shows a restricted range of composition and a sub-alkaline, tholeiitic affinity. They have low silica (41–48 wt % SiO_2) and potassium (0.2–0.9 wt % K_2O) contents with Al_2O_3 between 12.5 and 15.0 wt %, for a #Mg (molar [$MgO/MgO + Fe^{Tot}$]) of 38–65 (sample SZ290). In the TAS diagram, the studied granulite samples correspond to subalkaline, picro-basaltic to basaltic compositions (Fig. 5a). The low Si content of the studied samples can be interpreted as due to extraction of trondhjemitic melt during granulite facies metamorphism (Rossetti et al., 2010).

The following discrimination of the metabasalts is considered as tentative because of the extraction of an unknown amount of melt. According to Irvine and Baragar (1971) and Winchester and Floyd (1976), the granulite protolith can be classified as tholeiitic (Fig. 5b–c). The rare earth element patterns show LREE depletion with a slight convex-upward distribution ($[Gd/Yb]_N$ 0.9–1.5) and no Eu anomaly. The $(La/Sm)_N$ values are low (0.7–1.0) and their HREE concentrations range between 30 and 50 times

SED
3, 477–526, 2011

chondritic values for the preserved samples and around 10 times for sample SZ290. Such a pattern is close to those of N-MORBs (Fig. 6a; cf. Arevalo and McDonough, 2010). On a MORB-normalized diagram, the fluid-mobile LILE widely scatter widely, and element ratios based on them show little or no systematic behaviour. On the other hand, the fluid immobile trace elements show flat patterns compatible with a MORB signature (Fig. 6b). The samples display Nb/La values between 0.5 and 1.3 and in a plot of $(La/Sm)_N$ vs. Nb/La (after John et al., 2003; not shown), the samples are far from the arc magmatism fields and fall in-between the back-arc and MORB ones. Values of Th/Yb range between 0.07 and 0.16, Nb/Yb between 0.96 and 1.60, and TiO_2/Yb between 0.41 and 0.45. These values strongly resemble those of average N-MORB (see Pearce, 2008). In a Sr/Y vs. $(La/Sm)_N$ diagram (after Berger et al., 2099), the granulites have a Sr/Y ratio significantly lower than in intra-oceanic arc lavas (exemplified by Caribbean Cretaceous lava); they plot close to the fields of MORB-type lavas (Fig. 7a). In geotectonic discrimination diagrams based on "immobile" elements for basaltic rocks, majority of thesamples plot in the MORB/back-arc fields (Fig. 7b–c).

5 Mineral chemistry

The chemical compositions of minerals were determined using a CAMECA SX100 electron microprobe at the Institute für Mineralogie of Universität Stuttgart. Electron microprobe analyses (EMPA) were carried out in focused beam mode at 15 kV and 15 nA, using natural minerals and synthetic phases as standards. Concentration map for major elements (Ca, Fe, Mg, Mn, Al, Na) were also produced by stepwise movement of the thin section under the electron beam. Mineral recalculation and estimation of Fe^{3+} content were made using the AX2000 program in the THERMOCALCv.3.26 package (Holland and Powell, 2008; ftp://www.esc.cam.ac.uk/pub/minp/thermocalc/).

SED
3, 477–526, 2011

5.1 Garnet

Representative garnet analyses are presented in Table 2a. Garnet is essentially almandine (38–52 mol %), but it shows a large variation in grossular (26–34 mol %) and pyrope (12–30 mol %) components; spessartine (1–7 mol %) is present in minor amounts only (Fig. 8a). Representative compositional profiles and X-ray compositional maps are shown in Fig. 9. Three main types of chemical zoning are recognised (cf. Spear, 1993): (i) prograde zoning documented by a more or less pronounced (core-to-rim) bell shaped spessartine profile and pyrope increase (Fig. 9a); (ii) flat chemical profiles with retrograde zoning (Mg decrease) in the rim regions (Fig. 9b); (iii) and composite patterns (Fig. 9c). In type (ii), a rimward increase of the grossular component is observed, largely compensated by a decrease of the pyrope content. In garnet with outlines pointing to major resoprtion, the rimward chemical zoning is also typified by an increase in X_{Fe} values in conjunction with spessartine increase. Flat chemical profiles are typified by the lower spessartine and higher pyrope contents. Mg-rich garnet is generally related to temperature close to peak metamorphic conditions (e.g. Spear and Selverstone, 1983), being in line with the flat chemical profile (e.g., Spear, 1993; Ganguly, 2002). A similarly high Mg content occurs at the rim of the progradely zoned garnets that we thus attribute to the metamorphic peak. The sharp increase of the Ca and decrease of Mg contents with flat Mn and Fe contents can be explained as due to garnet growth in presence of a Ca-rich melt phase, i.e. during cooling (e.g., Spear and Kohn, 1996). The general picture described above is also complicated by ion diffusion next to both inclusions and external matrix minerals. For example, in garnets from sample SZ290 a 100–150 µm wide zone with a sharp increase in Mg- and Fe- and depletion in Ca- and Mn-components is observed close to the clinopyroxene inclusions.

5.2 Clinopyroxene

Representative microprobe analyses and structural formula of clinopyroxene are reported in Table 2b. Composition is dominated by the diopside component

SED
3, 477–526, 2011

(49–60 mol %), with minor hedenbergite (10–30 mol %) and Ca-Tschermaks (2–18 mol %). Jadeite component is negligible (<0.05) (Fig. 8b). Clinopyroxene occurring both in matrix and as inclusions in garnet shows similar composition. In all of the samples, a significant chemical zoning is observed moving from core to rim, which is typified by an increase of the Ca and Mg contents concomitantly with a decrease of the Al content (Fig. 9). A large variation in the Ca-Tschermaks component is also evident in the NG353 sample, in which clinopyroxene inclusions hosted in garnet contain lower Al and Na, and higher X_{Fe} than the core of clinopyroxene dispersed in the matrix (Table 2b).

5.3 Plagioclase

Representative analyses are presented in Table 2c. Composition of plagioclase is distinctly different in the preserved and retrogressed rock types (Fig. 8c). In the first case (samples NG353 and NG421), all analysed plagioclase grains, regardless of their textural context (matrix, inclusions, leucosome) have andesine compositions ($An_{43-51}Ab_{50-56}Or_{0-1}$). In the second case, most of the plagioclase grains have been pseudomorphosed into an albite-prehnite symplectite (sample SZ290). Albite also occurs as constituent of symplectite or in corona structures around garnet (sample EG354D). In several cases, matrix plagioclase shows alteration into prehnite.

5.4 Amphibole

Representative analyses of amphibole are given in Table 2d. In all samples, the composition of amphibole corresponds to tschermakite according to Leake et al. (2004) classification. In particular, amphibole from NG353 sample occurring in the matrix has the same composition as in the kelyphite structures around garnet and replacing clinopyroxene ($X_{Mg} = Mg/(Mg + Fe^{2+})$. On the other hand, coarse amphibole from sample SZ290 dispersed in the matrix shows higher X_{Mg} content (up to 0.88). Amphibole occurring as inclusion in garnet has been found in samples EG354D and NG353. It

SED
3, 477–526, 2011

has a similar composition with respect to the ones found in matrix (just smaller X_{Mg} values. Late-stage, post-kinematic amphibole is actinolitic in composition (Fig. 8d).

5.5 Epidote

Epidote was found both as inclusion (sample NG353) in garnet and as constituent of the late retrogressive matrix assemblage. Matrix epidote is rich in pistacite ($X_{Ps} = (Fe^{3+}/Fe^{3+} + Al)$ up to 0.38) with respect to epidote inclusion ($X_{Ps} = 0.05$).

6 Metamorphic evolution and reaction history

The petrographic and textural features described above show that five main metamorphic stages (M_1 to M_5) can be recognised in the Sabzevar ganulites. This metamorphic evolution is primarily derived from the inclusion assemblages hosted in the garnet cores and clinopyroxene grains in samples NG353 and NG421, and by the reaction textures overprinting peak assemblages in samples SZ290 and EG354D.

The M_1 stage corresponds to the early prograde metamorphic history that is typified by the inclusion assemblage found in the garnet, i.e. it predates the main episode of garnet growth. The assemblage comprises $Amp_1 + Pl_1 + Qz + Ttn_1 + Ep$. Probably formed in a later stage, Ilm_1 is also enclosed in Grt, and Ttn_1 completely pseudomorphed to $Ilm_1 + Cpx + Qtz$ (Fig. 4d). Replacement of Ttn_1 could have been due to the prograde reaction (Frost et al., 2000):

$$Amp + Ttn = Cpx + Qtz + Ilm + H_2O. \quad \text{(R1)}$$

The M_{2a} stage corresponds to the main phase of garnet growth close to the metamorphic peak and to the crystallisation of the matrix assemblage $Amp_2 + Pl_2 + Cpx_2 \pm Qtz$. In particular, presence of rutile in spiral trails of inclusions in the garnet rims reflects the prograde history during garnet growth, likely after destabilisation of matrix Ttn_1 and

SED
3, 477–526, 2011

Ilm_1. This assemblage can be then tentatively ascribed to a reaction such as (Manning and Bohlen, 1991; Tropper et al., 2002; Page et al., 2003):

$$Czo + Ttn = Grs + Rt + Qz + H_2O. \quad \text{(R2)}$$

After the main Grt growth episode, Ilm_2 crystallized at the expense of rutile in the matrix in association with Cpx_2, $Amph_2$, Grt, and $Plag_2$ (stage M_{2b}). This assemblages typifies the main equilibrium assemblage observed in fresh and unaltered granulite.

Crystallisation of the granulitc garnet-clinopyroxene-amphibole matrix is associated with leucosomes segregations. Leucosome textures such as those described in this study show striking similarities with those reported in Hartel and Pattison (1996), who interpreted the quartz + plagioclase leucosomes as melt textures produced by partial melting and hence product of migmatisation. In particular, the skeletal nature of the quartz and the plagioclase + quartz films, argue for an internal origin of such melts (see Rossetti et al., 2010). Hence, the M_2 stage involves amphibole dehydratation melting during prograde granulite facies migmatisation of a basic protolith according to the following generalised reaction (Hartel and Pattison, 1996):

$$Amp + Pl = Grt + Cpx + Ttn + \text{trondhjemitic melt}. \quad \text{(R3)}$$

Accordingly, the metamorphic stage M_2 is related to granulite formation associated with minor melt segregation.

M_2 was followed by development of M_3 symplectitic amphibole, plagioclase, quartz ± ilmenite forming coronas around garnet and clinopyroxene associations. The observed reaction texture indicate garnet-consuming reaction such as (Mengel and Rivers, 1991; Willard and Adams, 1994; Zaho et al; 2000)

$$Grt + Cpx + Qz + \text{fluid} \rightarrow Amp + Pl \pm Mag. \quad \text{(R4)}$$

Progress of this reaction needs fluid supply probably in response to external fluid infiltration during the uplift and related retrogressive evolution (Shervais et al., 2003; Engvik et al., 2007). Development of amphibole+plagioclase kelyphites around garnet

SED
3, 477–526, 2011

have been observed in many granulite terranes and is generally related to a predominantly isothermal decompression after metamorphic peak (e.g. Harley, 1989; Carswell, 1990; Thost et al., 1991; O'Brien, 1997). In addition, growth of matrix ilmenite at the expense of rutile indicates retrogression of the HP assemblage according the bulk reaction (Zhao et al., 2001):

$$\mathrm{Grt} + \mathrm{Rt} \rightarrow \mathrm{Ilm} + \mathrm{Pl} + \mathrm{Qz}. \quad \text{(R5)}$$

This reaction is mainly pressure-dependent and proceeds to the right with decompression (Liu et al., 1996, 1998).

Locally, a M_4 metamorphic assemblage of $\mathrm{Amp}_4 + \mathrm{Ep} \pm \mathrm{Chl}$ statically grew. This assemblage formed at the expense of Grt, Cpx, and $\mathrm{Amph}_{1\text{-}2\text{-}3}$, indicating the following bulk reaction (Abbott and Greenwood, 2001):

$$\mathrm{Cpx} + \mathrm{Grt} + \mathrm{Amp} + \mathrm{Pl} + \mathrm{fluid} + \mathrm{O_2} \rightarrow \mathrm{Amp_4} + \mathrm{Ep} + \mathrm{Chl} + \mathrm{Ab}. \quad \text{(R6)}$$

The latest stage of retrograde metamorphism is represented by the occurrence of M_5 cross-cutting prehnite-bearing veins.

7 Thermobarometry

To assess the *P-T* evolution of the Sabzevar granulites, inverse and forward modelling techniques were integrated (cf. Powell and Holland, 2008). Inverse modelling combines conventional (single-reaction) thermobarometry with multiple reactions thermobarometry applying the THERMOCALC software (3.26 version) and its internally-consistent thermodynamic data set (Holland and Powell, 1998; Powell and Holland, 2008). Conventional thermobarometry includes Grt-Cpx-Pl-Qz (GADS barometry; Perkins Newton, 1982; Eckert et al., 1991) and Grt-Amp-Pl-Qz (Kohn and Spear, 1990) barometry for pressure estimates; as well as the Mg-Fe exchange for the both the Grt-Cpx (Ellis and Green, 1979; Krogh Ravna, 2000a) and Grt-Amp (Krogh Ravna, 2000b) pairs, and the Zr-in rutile (Zack et al., 2004; Watson et al., 2006; Ferry and Watson, 2007;

SED
3, 477–526, 2011

Tomkins et al., 2007) thermometry for temperature estimates. For what concerns the Zr-in rutile thermometry (see below), calibrations by Watson et al. (2006), Ferry and Watson (2007) and Tomkins et al. (2007) gave similar results, whereas results from Zack et al. (2004) were systematically 100 °C higher, and were not thus taken into account in this study. Both phase diagram and the average *P-T* THERMOCALC calculations mode have been applied, considering mineral data activities calculated by the AX program enclosed in the THERMOCALC package. For average pressure and temperature estimates, we only considered calculations showing a statistical consistency as expressed by the "*sigfit*" coefficient (Powell and Holland, 1994).

The *P-T-X* modelling of the Sabzevar granulites during the M_1-to-M_2 composite metamorphic evolution was computed using the Perple_X_07 software (Connolly, 2005; http://www.perplex.ethz.ch, v. 6.6.5, downloaded 7 January 2011). Because of the unknown amount of melt extracted from the rock, the calculation is considered as tentative and, accordingly, results on *P-T* conditions as semi-quantitative.

7.1 Inverse modelling

7.1.1 M_1 stage

For this early metamorphic stage, characterized by the assemblage made of amphibole, epidote, and titanite + garnet, lower amphibolite facies conditions can be assumed.

7.1.2 M_{2a} stage

Prograde conditions were calculated using the composition of $Amp_1 + Pl_1 + Ilm_1 + Ttn_1$ (+Qz) inclusion assemblages hosted within the core domain of the garnet. Average THERMOCALC *P-T* estimates span for sample NG353 are 644 ± 117 °C, 0.8 ± 0.1 GPa. On the same assemblages, the amphibole-garnet thermometry of Krogh Ravna (2000b) gives results 640–750 °C.

SED
3, 477–526, 2011

7.1.3 M_{2b} stage

The progressive transition to the M_{2b} stage is related to growth of garnet in association with rutile. Peak conditions were calculated using the composition of (i) Cpx + Pl + Rt ± Ilm (+Qz) inclusions within the rim domain of the garnet and (ii) Grt-Cpx-Pl-Amp matrix assemblages showing textural equilibrium. The average *P*-*T* calculations as obtained with THERMOCALC cluster around 750–850 °C and 1.0–1.2 GPa. A significantly lower temperature but similar pressure is calculated taking into account the outer, Ca-rich garnet domains (Fig. 10). The Grt-Cpx thermometry of Krogh Ravna (2000a) and Ellis and Green (1979) (calculated for an average $P = 1.0$ GPa for all samples) gave similar results, in the order of 715–765 °C. Using the composition of clinopyroxene with highest Al contents (in the rims) for the assemblage indicated above, calculated conditions are about 50–100 °C higher, suggesting that peak *T* was higher than obtained by the applied thermometers due to post-peak re-equilibration of clinopyroxene. The GADS barometry of Perkins Newton (1982) and Eckert et al. (1991) gave pressure estimates of 1.1–1.2 GPa for samples NG353, EG354, and NG421, and 1.3 GPa for sample SZ290 (at an average $T = 750$ °C for all samples), respectively. The Zr-in rutile thermometry from rutile grains hosted in the garnet rim domains provides 710–800 °C (Fig. 10).

7.1.4 M_3 stage

The garnet-amphibole thermometry of Krogh Ravna (2000b) calibration has been tentatively applied to garnet rim composition in equilibrium with amphibole occurring in the corona structures and amphibole large grain. As expected, temperature estimates are lower than for M_2: 611–677 °C for sample NG353, and 574–631 °C for sample EG354. For all samples, the highest values were obtained when amphibole with higher X_{Mg} is chosen. The pressure conditions were calculated by the application of the Kohn and Spear (1990) calibration on the amphibole and plagioclase occurring in symplectite and corona structures in textural equilibrium with garnet rims. Results, calculated in the range from 500 ° to 700 °C, span from 0.35 to 0.62 GPa.

SED
3, 477–526, 2011

7.1.5 M_4-to-M_5 stage

The late retrogressive *P-T* conditions have been only qualitatively inferred by using the stability fields for the considered mineral assemblage. The presence of lately-formed actinolite, chlorite, epidote, albite and prehnite-zeolite assemblages collectively indicate that final equilibration occurred under greenschist-to-sub-greenschist facies *P-T* conditions. In particular, the late prehnite-bearing veins attest for the final M_5 stage occurred at temperature conditions between 200 and 280 °C for pressure less than 0.3 GPa. Furthermore, presence of wairakite-free zeolitic assemblages (heulandite) poses an upper limit for the temperature and pressure conditions during M_5 ($T < 250$ °C and $P < 0.2$ GPa; Frey et al., 1991).

7.2 Forward modelling

Pseudosections in the NCFMASHTMnO (Na_2O-CaO-FeO-MgO-Al_2O_3-SiO_2-H_2O-TiO_2-MnO-O_2) chemical system were calculated for the composition of sample NG421 (Table 1), containing garnet with only minor indication for corrosion. The following solid solution mixing models offered by Perple_X were considered in the calculations (details in solut09.dat; PERPLEX 07; database: hp04ver.dat): Amph(DPW) for amphibole, Grt(HP) for garnet, Cpx(HP) for clinopyroxene, feldspar for feldspar, melt(HP) for the melt phase, and H_2O for the fluid phase; rutile and ilmenite were considered as pure phases. The small amount of whole rock K_2O has been neglected because the current amphibole mixing models do not consider K-bearing end-members. For the calculations, water and O_2 content were fixed to 1 (close to the measured value) and 0.01 wt %, respectively. A representative pseudosection is shown in Fig. 11a.

The most important parameters to reconstruct the *P-T* history of the Sabzevar granulites are the garnet compositions, the inclusion assemblages in garnet, and the distribution of Ti-bearing phases, with titanite, ilmenite and rutile growth tracing the different stages in the metamorphic evolution.

SED
3, 477–526, 2011

The M_1 episode, predating major garnet growth, is characterized by the presence of large titanite. A tentative Perple_X calculation considering H_2O-satured conditions results (not shown here) is a (fluorine-free) titanite stability field at low T conditions (<450 °C). The presence of titanite is consistent with small modal amounts of garnet (<3 %) at such conditions. This early formed M_1 garnet incorporated most of the Mn available in the rock, and can still be recognized as garnet core (Fig. 9).

To trace the prograde path towards the M_2 peak, particularly significant are boundaries between the Ti-mineral phases and the fact that garnet growth is pressure sensitive (Fig. 11b). The calculations show that a relatively narrow reaction field of coexisting ilmenite and rutile exists, bounding a low-pressure, Ilm-bearing field from a high-pressure, Rt-bearing one (Fig. 11a). The textural evidence documenting rutile being lately formed with respect to ilmenite (Ilm_1) indicates pressure increase. The recorded M_{2a} step of the metamorphic history is assumed to be preserved close to garnet cores that record the prograde chemical zoning (Fig. 9a–c). These are characterized by a Mg content of ca. 0.45 c.f.u., Ca of ca. 0.7 c.f.u., and inclusions of $ilmenite_1$. Because of the presence of ilmenite, conditions of about 0.7 GPa and 650–680 °C are estimated for the M_{2a} stage (Fig. 11a). These estimates are in line with those obtained from inverse thermobarometry (Fig. 10). Transition from M_{2a} to M_{2b} is typified by crystallisation of garnet rim domains with dominant rutile. An inner rim of garnet representing M_{2b} contains inclusions of rutile, higher Mg content (up to 0.6 c.f.u.) and a nearly constant Ca content. These data indicate an increase in P accompanied by minor heating along a path nearly parallel to the Ca isopleths. The estimated peak conditions of this M_2 step attained at ca. 780 °C and 1.1–1.2 GPa, limited by the upper pressure stability of plagioclase. Also in this case, results are in good accordance with the Zr-in-rutile thermometry and the THERMOCALC calculations (Fig. 11a). Achievement of the peak P-T conditions during M_{2b} was accompanied with production of a small amount melt that is now visible as leucosomse. Subsequent cooling resulted in resorption of garnet that is also indicated by Mn-rich seems (Fig. 9c), at first within the rutile stability field and then within the ilmenite field. An important constraint on the P-T path can

SED
3, 477–526, 2011

be derived from garnet with zoning pattern such as Ng353_grt1 (Fig. 9b). This garnet type is facing into a leucosome rim and shows little resorption. Its outer rim zoning is characterized by a significant increase in Ca (up to 0.9 c.f.u.), compensated be a decrease in Mg. Obviously, in this case the garnet outer rim adjacent to melt grew during cooling instead of being resorbed. Considering the calculated modal abundance of garnet, this feature requires nearly isobaric cooling, compatible with an anti-clockwise *P-T* path (Fig. 11a). In the rock matrix, ilmenite almost completely replaced rutile. It only survived as shielded (mainly mono-phase) inclusion garnet or in larger ilmenite aggregates. The cooling path is also imposed by the preservation of plagioclase in the matrix assemblages (Fig. 11a).

Crystallisation of Ttn_2 in leucosomes likely occurred close to the solidus during cooling. In contrast to early formed, relatively low-*T* Ttn_1, the Ttn_2 stability during this episode probably extended to significantly higher temperature because of the presence of significant amounts of fluorine in the residual melt (Tropper et al., 2002; Troitzsch and Ellis, 2002).

Because for the calculation of the pseudosection water content is fixed to 1 wt %, resulting subsolidus assemblages are mostly water-deficient, "dry" assemblages which cannot account for retrograde reactions in retrogressed samples, where minerals such as epidote, chlorite, actinolite, prehnite and zeolite appear. A Perple_X calculation of subsolidus phase relation with water-saturated conditions (not shown here) shows that during cooling epidote appears in the range of 550 °C during cooling. This temperature range fixes conditions for the composite M_3–M_4 retrogression.

8 Discussion

8.1 *P-T* path: proposal of an anticlockwise trajectory

The metamorphic evolution reconstructed from the Sabzevar granulites attests for an early prograde stage starting from amphibolite-facies conditions (M_1 stage) with final

SED
3, 477–526, 2011

equilibration under granulite-facies peak conditions (M_2 stage). The peak mineral assemblage described in this study (Grt + Cpx + Pl + Rt ± Amp ± Qz) is indicative of the Opx-free HP granulite facies (Pattison, 2003; O'Brien and Rötzler, 2003). According to thermobarometric calculations, peak metamorphism occurred at ca. 780 °C and 1.1–1.2 GPa, as indicated by assemblage M_2. This is compatible with (i) occurrence of rutile and garnet in MORB-like rocks, which indicate minimum pressure of about 0.1–0.12 GPa (Ernst and Liu, 1998); and (ii) presence of Cpx instead of Opx (e.g. O'Brien and Rötzler, 2003). Calculated peak *P-T* conditions are also compatible with partial melting of amphibolite as they are located above the H_2O-saturated basaltic solidus (Vielzieuf and Schmidt, 2001).

Textural evidence for in situ amphibolite dehydratation melting (see also Rossetti et al., 2010) attests for migmatisation occurring during this prograde history and during attainment of the granulite climax. The nearly isobaric late-M_2 cooling documented by the pseudosection calculations based on the Ca-rich outer garnet rims (Fig. 11) and the ilmenite-bearing matrix assemblage collectively suggest a counterclockwise *P-T* loop (pressure axis upward; Fig. 12) within a prograde Barrovian-type metamorphic gradient (in the order of 25 °C km^{-1}). The metamorphic peak was followed by a polyphase metamorphic retrogression (M_3-to-M_5 stages), tracing the progressive cooling and exhumation from upper-greenschist/amphibolite facies (assemblage M_3) down to the stability field of prehnite and zeolite (assemblage M_5) (Fig. 12).

8.2 A possible geodynamic scenario

The geochemical data presented above document that the Sabzevar granulites likely derive from a MORB-type precursor and therefore represent remnants of a former oceanic crust affected by a Early Cretaceous (Albian) subduction zone metamorphism. The thermobarometric estimates of peak metamorphism demonstrate incipient migmatisation of the oceanic protolith already at relatively shallow depths (ca. 40 km) and hence argue for a high heat flow subduction channel.

SED
3, 477–526, 2011

Forward modelling of the thermal and rheological structure of subduction zones as well as fossil and active examples of oceanic subduction zones (e.g., Peacock et al., 1994, 2005; Peacock and Wang, 1999; Hacker et al., 2003; Conder., 2005; Bebout et al., 2007; Casco et al., 2008; Guilmette et al., 2008) have documented that cool geothermal conditions can not be generalized to any oceanic subduction and that "warmer" geothermal environments such as those documented in this study do not necessarily require an atypical tectonic environment. The most favourable conditions for a hot subduction setting pertain to slab edges and windows (Kincaid and Griffiths, 2004; Thorkelson and Breitsprecher, 2005), subhorizontal or flat subduction (Gutcher et al., 2000), onset of subduction (e.g., Gerya et al., 2002), or subduction of a young slab or of a ridge (e.g. Peacock et al., 1994; Peacock, 1996; Okudaira and Yoshitake, 2004). High heat-flow subduction settings also provide appropriate conditions to cause slab melting and generate the tonalite-trondhjemite-granodiorite magmatic suites (Martin et al., 2005, and references therein). Peacock et al. (1994) documented that young (0–5 Ma) crust that is slowly subducting (1 cm yr^{-1}) into a hot mantle at constant shear may produce a subduction zone metamorphism with high T/P ratios and peak metamorphic conditions compatible with those of the Sabzevar HP granulites and typical of most dynamothermal soles in ophiolites (Jamieson, 1986; Spray, 1984; Peacock, 1987; Wakabayashi and Dilek, 2000). Peacock et al. (1994) also showed that aging of a nascent subduction zone rapidly results in cooling of the subducted crust and shifting the metamorphic gradient towards higher P/T ratios. We thus propose that the anticlockwise P-T trajectory followed by the Sabzevar granulites is the record of a progressively colder thermal regime within the subduction channel in consequence of the continuous underthrusting of the oceanic material at the subduction front.

Following reconstruction presented in Rossetti et al. (2010), this oceanic subduction can be referred to a former (likely Early Cretaceous in age) oceanic branch (hereafter referred as Proto-Sabzevar Ocean to distinguish it from the later formed Sabzevar Ocean) that can be tentatively linked to the Sistan Ocean to the East of the CEIM (cf. Tirrull et al., 1983; McCall, 1997), where Early Cretaceous subduction zone

SED
3, 477–526, 2011

metamorphism is documented (Footohi Rad et al., 2009). In this scenario, closure of the Sistan Ocean occurred along a diachronic suture that conformed to two different geothermal gradient conditions, $<10\,^{\circ}C\,km^{-1}$ (the older, ca. 125 Ma, Sistan eclogites; Fotoohi Rad et al., 2009) to $20–25\,^{\circ}C\,km^{-1}$ (Sabzevar granulites). We speculate that this might have been consequence of the along-strike termination of the Sistan subduction, since slab edges provide favourable geodynamic conditions for hot subduction settings and hence the appropriate petrogenetic mechanisms to cause slab melting (Kincaid and Griffiths, 2004; Thorkelson and Breitsprecher, 2005). Alternatively, the proto-Sabzevar ocean can be interpreted as small marginal basin formed in the upper-plate of the Neothetyan subduction, separated from the Sistan Ocean and with an independent evolution. Apart the interpretation adopted, by integrating our reconstruction with the tectono-metamorphic evolution of the Neotehyan subduction along the Sanandaj-Sirjan Zone as reconstructed in the work of Agard et al. (2006), we propose that Early Cretaceous oceanic subduction systems along the Sabzevar/Sistan-Zagros transect conformed to different geothermal gradient conditions, testifying for occurrence of low (conduction-dominated; Proto-Sabzevar subduction) and high (advection-dominated; Neotheyan and Sistan subduction) thermal Peclet number (cf. Faccenna et al., 2001; Sandiford, 2002) subduction channels. This evidence also suggests a heterogeneous distribution in the mode and style of oceanic subduction in the upper plate of the subducting Neo-Thetyan ocean, likely consequence of the different types of oceanic lithosphere (mature ocean vs. back-arc lithosphere) under consumption.

9 Conclusions

The geochemical and petrological study of the Sabzevar H*P* granulites provide new insights on the tectono-metamorphic evolution experienced by the remnants of peri-Tethyan oceanic branches that surround the CEIM (Fig. 1). In particular, evidence for a nascent oceanic subduction zone in central Iran (Sabzevar structural zone) during the Early Cretaceous is documented.

SED
3, 477–526, 2011

Based on the regional scenario, our results suggest that punctuated events of subduction of short-lived marginal oceanic domains accompanied the long-lasting (Mesozoic-to-Tertiary) history of the Neotethyan subduction along the Sananday-Sirjan zone. Consequently, diachronic and independent tectonic evolutions of the different ophiolitic domains surrounding the CEIM have to be necessarily taken into account for future investigations.

Acknowledgements. We thank Amir and Habib for assistance during field work. D. Cozzupoli participated to the field work and is thanked for useful discussion together with H. J. Massonne, C. Faccenna and M. Mattei.

References

Abbotto, R. N. and Green Wood, J. P.: Retrograde metamorphim of eclogite in the Southern Appalachian Mountains, U.S.A., a case involving seamount subduction?, J. Metamorph. Geol., 19, 433–443, 2001.

Agard, P., Monie, P., Gerber, W., Omrani, J., Molinaro, M., Labrousse, L., Vrielynck, B., Meyer, B., Jolivet, L., and Yamato, P.: Transient synobduction exhumation of Zagros blueschists inferred from pressure, temperature, deformation, time and kinematic constraints: Implications for Neotethys wedge dynamics, J. Geophys. Res., 111, B11401, doi:10.1029/2005JB004103, 2006.

Agard, P., Yamato, P., Jolivet, L., and Burov, E.: Exhumation of oceanic blueschists and eclogites in subduction zones: timing and mechanisms, Earth-Sci. Rev., 92, 53–79, 2009.

Alavi-Tehrani, N.: Geology and petrography in the ophiolite range NW of Sabzevar, Khorasan/Iran with special regards to metamorphism and genetic relations in an ophiolite suite, Geological Survey of Iran, Rep. No. 43, 1977.

Arevalo Jr., R. and McDonough, W. F.: Chemical variations and regional diversity observed in MORB, Chem. Geol., 271, 70–85, 2010.

Bagheri, S., and Stampfli, G. M.: The Anarak, Jandaq and Posht-e-Badam metamorphic complex in central Iran: New geological data, relationships and tectonic implications, Tectonophysics, 451, 123–155, 2008.

SED

3, 477–526, 2011

Baroz, F., Macaudiere, J., Montigny, R., Noghreyan, M., Ohnenstetter, M., and Rocci, G.: Ophiolites and related formations in the central part of the Sabzevar (Iran) and possible geotectonics reconstructions, Neues J. Geol. Paläont. Abh., 168, 358–388, 1984.
Bebout, G. E., Ryan, J. G., Leeman, W. P., and Bebout, A. E.: Fractionation of trace elements by subduction-zone metamorphism: effect of convergent-margin thermal evolution, Earth Planet. Sc. Lett., 171, 63–81, 2007.
Beccaluva, L., Di Girolamo, P., Macciotta, G., and Morra, V.: Magma affinities and fractionation trends in ophiolites, Ofioliti, 8, 307–324, 1983.
Berger, J., Caby, R., Liégeois, J. P., Mercier, J. C. C., and Demaiffe, D.: Dehydration, melting and related garnet growth in the deep root of the Amalaoulaou Neoproterozoic magmatic arc (Gourma, NE Mali), Geol. Mag., 146(2), 173–186, 2009.
Besse, J., Torcq, F., Gallet, Y., Ricou, L. E., Krystyan, L., and Saidi, A.: Late Permian to late Triassic paleomagnetic data from Iran: constraints on migration of the Iranian block through the Tethyan ocean and initial destruction of Pangea, Geophys. J. Int., 135, 77–92, 1998.
Brown, M.: Duality of thermal regimes is the distinctive characteristic of plate tectonics since the Neoarchean, Geology, 34, 961–964, 2006.
Brown, M.: Paired metamorphic belts revised, Gondwana Res., 18, 46–59, 2010.
Bucher, K. and Frey, M.: Petrogenesis of Metamorphic Rocks, 7th edn., Springer-Verlag, Berlin, 2002.
Carswell, D. A.: Eclogites and eclogite facies: definitions and classification, in: Eclogite Facies Rocks, edited by: Carswell, D. A., Blackie, London, 219–221, 1990.
Cawood, P. A., Kröner, A., Collins, W. J., Kusky, T. M., Mooney, W. D., and Windley, B. F.: Accretionary orogens through Earth history, in: Earth Accretionary Systems in Space and Time, edited by: Cawood, P. A. and Kröner, A., J. Geol. Soc. London, Special Publication, 318, 1–36, 2009.
Coleman, R. G., Lee, D. E., Beatty, L. B., and Brannock, W. W.: Eclogites and eclogites: their differences and similarities, Geol. Soc. Am. Bull., 76, 483–508, 1965.
Conder, J. A.: A case for hot slab surface temperatures in numerical viscous flow models of subduction zones with an improved fault zone parameterization, Phys. Earth Planet. In., 149, 155–164, 2005.
Connolly, J. A. D.: Computation of phase equilibria by linear programming: a tool for geodynamic modeling and its application to subduction zone decarbonation. Earth Planet. Sc. Lett., 236, 524–541, 2005.

SED
3, 477–526, 2011

Delaloye, M. and Desmons, J.: Ophiolites and mélange terranes in Iran. A geochronological study and paleotectonic implications, Tectonophysics, 68, 83–111, 1980.
Dercourt, J., Gaetani, M., Vrielynck, B., Barrier, E., Biju-Duval, B., Brunet, M. F., Cadet, J. P., Crasquin, S., and Sandulescu, M. (Eds.): Atlas Peri-Tethys Paleoegeographical Maps, vol. I–XX. CCGM/CGMW, Paris, 24 maps and explanatory note, 1–269, 2000.
Dewey, J. F. and Bird, J. M.: Mountain belts and the new global tectonics, J. Geophys. Res., 75, 2625–2647, 1970.
Eckert, J. O., Newton, R. C., and Kleppa, O. G.: The ΔH of reaction and recalibration of garnet-pyroxene-plagioclase-quartze geobarometers in the CMAS system by solution calorimetry, Am. Mineral., 76, 148–160, 1991.
Ellis, D. J. and Green, D. H.: An experimental study of the effect of Ca upon garnet-clinopyroxene Fe-Mg exchange equlibria, Contrib. Mineral. Petr., 71, 13–22, 1979.
Engvik, A. K., Tveten, E., Bingen, B., Viola, G., Erambert, M., Feito, P., and De Azavedo, S.: P-T-t evolution and textural evidence for decompression of Pan-African high-pressure granulites, Lurio Belt, north-eastern Mozambique, J. Metamorph. Geol., 25, 935–952, 2007.
Ernest, W. G. and Liu, J.: Experimental phase-equilibrium study of Al- and Ti-contents of calcic amphibole in MORB-A semiquantitative thermobarometer, Am. Mineral., 83, 952–969, 1998.
Faccenna, C., Becker, T. W., Lucente, F. P., Jolivet, L., and Rossetti, F.: History of subduction and Back-arc extension in the Central Mediterranean, Geophys. J. Int., 145, 809–820, 2001.
Ferry, J. and Watson, E. B.: New thermodynamic models and revised calibrations for the Ti-in-zircon and Zr-in-rutile thermometers, Contrib. Mineral. Petr., 154, 429–437, 2007.
Fotoohi Rad, G. R., Droop, G. T. R., and Burges, R.: Early Cretaceous exhumation of high-pressure metamorphic rocks of the Sistan Suture Zone, eastern Iran, Geol. J., 44, 104–116, 2009.
Frey, M., De Capitani, C., and Liou, J. G.: A new petrogenetic grid for low-grade metabasites, J. Metamorph. Geol., 9, 479–509, 1991.
Frost, B. R., Frost, C. D., Hulsebosch, T. P., and Swapp, S. M.: Origin of the charnockites of the Louis Lake batholith, Wind River Range, Wyoming, J. Petrol., 41, 1759–1776, 2000.
Ganguly, J.: Diffusion kinetics in minerals: principles and applications to tectono-metamorphic processes, EMU notes in Mineralogy, 4(chapter 10), 271–309, 2002.
García-Casco, A., Lázaro, C., Torres-Roldán, R. L., Núñez Cambra, K., Rojas Agramonte, Y., Kröner, A., Neubauer, F., Millán, G., and Blanco Quintero, I.: Partial melting and counter-clockwise P-T path of subducted oceanic crust (Sierra del Convento mélange, Cuba), J.

SED
3, 477–526, 2011

Petrol., 49(1), 129–161, 2008.
Garrido, C. J., Bodinier, J. L., Burg, J. P., Zeilinger, G., Hussain, S. S., Dawood, H., Chaudhry, M. N., and Gervilla, A. F.: Petrogenesis of mafic garnet granulites in the lower crust of the Kohistan palaeoarc complex (Northern Pakistan): Implications for intracrustaldifferentiation of island arcs and generation of continental crust, J. Petrol., 47, 1873–1914, 2006.
Gerya, T. V., Stoeckhert, B., and Perchuk, A. L.: Exhumation of high-pressure metamorphic rocks in a subduction channel: a numerical simulation, Tectonics, 21(6), 1056, doi:10.1029/2002TC001406, 2002.
Ghasemi, A. and Talbot, C. J.: A new tectonic scenario for the Sanandaj-Sirjan Zone (Iran), J. Asian Earth Sci., 26, 683–693, 2006.
Golonka, A. J.: Plate tectonic evolution of the southern margin of Eurasia in the Mesozoic and Cenozoic, Tectonophysics, 381, 235–273, 2004.
Guilmette, C., Hebert, R., Dupuis, C., Wang, C., and Li, Z.: Metamorphic history and geodynamic significance of high-grade metabasites from the ophiolitic mélange beneth the Yarlung Zangbo ophiolites, Xigaze area, Tibet, J. Asian Earth Sci., 32, 423–437, 2008.
Gutcher, M. A., Maury, R., Eissen, J. P., and Bourdon, E.: Can slab melting cuased by flat subduction?, Geology, 28, 535–538, 2000.
Hacker, B. R., Abers, G. A., and Peacock, S. M.: Subduction Factory 1. Theoretical mineralogy, densities, seismic wave speeds, and H_2O contents, J. Geophys. Res., 108, 2029, doi:10.1029/2001JB001127, 2003.
Harly, S. L.: The origin of granulites: A metamorphic perspective, Geol. Mag., 126, 215–247, 1989.
Hartel, T. H. D. and Pattison, D. R. M.: Genesis of the Kapuskasing (Ontario) migmatitic mafic granulites by dehydration melting of amphibole: the importance of quartz to reaction progress, J. Metamorph. Geol., 14, 591–611, 1996.
Hoffman, E. L.: Instrumental Neutron Activation in Geoanalysis, J. Geochem. Explor., 44, 297–319, 1992.
Holland, T. J. B. and Powell, R.: An internally consistent thermodynamic data set for phases of petrological interest, J. Metamorph. Geol., 16, 309–343, 1998.
Irvine, T. N. and Baragar, W. R. A.: A guide to the chemical classification of the common volcanic rocks, Can. J. Earth Sci., 8, 523–548, 1971.
Jamison, R. A.: P-T path from high temperature shear zones beneath ophiolites, J. Metamorph. Geol., 4, 3–22, 1986.

SED
3, 477–526, 2011

John, T., Schenk, V., Haase, K., Scherer, E., and Tembo, F.: Evidence for a Neoprotrozoic ocean in south-central Africa from mid-ocean ridge type geochemical signature and pressure temperature estimates of Zambian eclogites, Geology, 31(3), 243–246, 2003.
Jolivet, L., Faccenna, C., Goffe, B., Burov, E., and Agard, P.: Subduction tectonics and exhumation of high-pressure metamorphic rocks in the Mediterranean orogens, Am. J. Sci., 303, 353–409, 2003.
Kincaid, C. and Griffiths, R. W.: Variability in flow and temperatures within mantle subduction zones. Geochem. Geophy. Geosy., 5, Q06002, doi:10.1029/2003GC000666, 2004.
Kohn, M. J. and Spear, F. S.: Two new geobarometers for garnet amphibolites, with applications to Southeastern Vermont, Am. Mineral., 75, 89–96, 1990.
Kretz, R.: Symbols for rock-forming minerals, Am. Mineral., 68, 277–279, 1983.
Krogh Ravna, E.: The garnet-clinopyroxene Fe-Mg geothermometer: an update calibration, J. Metamorph. Geol., 18, 211–219, 2000a.
Krogh Ravna, E.: Distribution of Fe and Mg between coexisting garnet and hornblende in synthetic and natural systems: an empirical calibration of the garnet – hornblende Fe-Mg geothermometer, Lithos, 53, 305–321, 2000b.
Kuno, H.: Differentiation of basalt magmas, in: Basalts: the Poldervaart treatise on rocks of basaltic composition, edited by: Hess, H. H. and Poldervaart, A. A., New York, Interscience, 2, 623–688, 1968.
Le Bas, M. J., Le Maitre, R. W., and Woolley, A. R.: The construction of the total alkali-silica chemical classification of volcanic rocks, Miner. Petrol., 46, 1–22, 1992.
Leake, B. E., Alan, R. W., William, D. B., Ernst, A. J. B., Giovanni, F., Jeol, D. J., Frank, C. H., Hanan, J. K., Vladimir, G. K., John, C. S., Nicholas, C. N. S., and Eric, J. W. W.: Nomenclature of amphiboles: Additions and revisions to the International Mineralogical Associations amphibole nomenclature, Am. Mineral., 89, 883–887, 2004.
Lensch, G., Mihm, A., and Alavi Tehrani, N.: Petrography and geology of the ophiolite belt north of Sabzevar Khorasan (Iran), Neues Jahrbuch Fur Geologie un Palaontologie Monatshefte, 131, 156–178, 1977.
Liou, J. G., Zhang, R., Ernst, W. G., Liu, J., and McLimans, R.: Mineral parageneses in the Piampaludo eclogitic body, Gruppo di Voltri, western Ligurian Alps, Schweiz. Miner. Petrog., 78, 317–355, 1998.
Liu, J., Bohlen, S. R., and Ernest, W. G.: Stability of hydrous phases in subducting oceanic crust, Earth Planet. Sc. Lett., 143, 161–171, 1996.

SED
3, 477–526, 2011

Mahèo, G., Bertrand, H., Guillot, S., Villa, I. M., Keller, F., and Capiez, P.: The south Ladakh ophiolites (NW Himalaya, India): an intraoceanic tholeiitic origin with implication for the closure of the Neo-Tethys, Chem. Geol., 203, 273–303, 2004.
Manning, C. E. and Bohlen, S. R.: The reaction titanite + kyanite = anortite + rutile and titanite-rutile barometry in eclogites, Contrib. Mineral. Petr., 109, 1–9, 1991.
Martin, H., Smithies, R. H. M., Rapp, R., Moyen, J. F., and Champion, D.: An overview of adakite, tonalite-trondhjemite-granodiorite (TTG) and sanukitoid: relationships and some implications for crustal evolution, Lithos, 79, 1–24, 2005.
McCall, G. J. H.: The geotectonic history o the Makran and adjacent area of Southern Iran, J. Asian Earth Sci., 15, 517–531, 1997.
Mengel, F. and Rivers, T.: Decompression relations and P-T conditions in high- grade rocks, Northern Labrador: P-T-t paths from individual samples and implications for Early Proterozoic tectonic evolution, J. Petrol., 32, 139–167, 1991.
Newton, R. C. and Perkins, D.: Thermodynamic calibration of geobarometers on the assemblage garnet-plagioclase-orthopyroxene (clinopyroxene)- quartz, Am. Mineral., 67, 203–222, 1982.
Niu, Y. L. and O'Hara, M. J.: MORB mantle hosts the missing Eu (Sr, Nb, Ta and Ti) in the continental crust: new perspectives on crustal growth, crust-mantle differentiation and chemical structure of oceanic upper mantle, Lithos, 112, 1–17, 2009.
O'Brien, P. J.: Garnet zoning and reaction textures in overprinted eclogites, Bohemian Massif, European Variscides: a record of their thermal history during exhumation, Lithos, 41, 119–133, 1997.
O'Brien, P. J. and Rötzler, J.: High-pressure granulites: Formation, Recovery of Peak Conditions and Implication for Tectonics, J. Metamorph. Geol., 21, 3–20, 2003.
Okudaira, T. and Yoshitake, Y.: Thermal consequences of the formation of a slab window beneath the Mid-Cretaceous southwest Japan arc: A 2-D numerical analysis, Isl. Arc, 13, 520–532, 2004.
Page, F. Z., Essene, E. J., and Mukasa, S. B.: Prograde and retrograde history of eclogites from the Eastern Blue Ridge, North Carolina, USA, J. Metamorph. Geol., 21, 685–698, 2003.
Pattison, D. R. M.: Petrogenetic significance of orthopyroxene – free garnet + clinopyroxene + plagioclase ± quartz-bearing metabasites with respect to amphibolite and granulite facies, J. Metamorph. Geol., 21, 21–34, 2003.
Peacock, S. M.: Creation and preservation of subduction-related inverted metamorphic

SED
3, 477–526, 2011

gradients, J. Geophys. Res., 92(12), 763–781, 1987.
Peacock, S. M.: Thermal and petrologic structure of subduction zones, in: subduction top to bottom, Geophysics Monoger. Geology, 21, 21–34, 1996.
Peacock, S. M. and Wang, K.: Seismic consequences of warm versus cool subduction zone metamorphism: examples from northeast and southwest Japan, Sience, 286, 937–939, 1999.
Peacock, S. M., Rushmer, T., and Thompson, A. B.: Partial melting of subducting oceanic crust, Earth Planet. Sc. Lett., 121, 227–244, 1994.
Peacock, S. M., van Keken, P. E., Holloway, S. D., Hacker, B. R., Abers, G., and Fergason, R. L.: Thermal structure of the Costa Rica-Nicaragua subduction zone: slab metamorphism, seismicity and arc magmatism, Phys. Earth Planet. Int., 149, 187–200, 2005.
Pearce, J.: Geochemical fingerprinting of oceanic basalts with applications to ophiolite classification and the search for Archean oceanic crust, Lithos, 100, 14–48, doi:10.1016/j.lithos.2007.06.016, 2008.
Pearce, J. A. and Cann, J. R.: Tectonic setting of basic volcanic rocks determined using trace element analyses, Earth Planet. Sc. Lett., 19, 290–300, 1973.
Perkins III., D. and Newton, R. C.: Charnockite geobarometers based on coexisting ganet-pyroxene-plagioclase-quartz, Nature, 292, 144–146, 1981.
Powell, R. and Holland, T.: Optimal geothermometry and geobarometry, Am. Mineral., 79, 120–133, 1994.
Powell, R. and Holland, T. J. B.: On thermobarometry, J. Metamorph. Geol., 26, 155–179, 2008.
Ricou, L. E.: Tethys reconstructed: plates, continental fragments and their boundaries since 260 Ma from Central America to South-eastern Asia, Geodin. Acta, 7, 169–218, 1994.
Rossetti, F., Nasrabady, M., Vignaroli, G., Theye, T., Gerdes, A., Razavi, S. M. H., and Moin Vaziri, H.: Early Cretaceous migmatitic mafic granulites from the Sabzevar range (NE Iran): implications for the closure of the Mesozoic peri-Tethyan oceans in central Iran, Terra Nova, 22, 26–34, 2010.
Sandiford, M.: Low thermal Peclet number intraplate orogeny in central Australia, Earth Planet. Sc. Lett., 201, 309–320, 2002.
Scambelluri, M., Müntener, O., Hermann, J., Piccardo, G. B., and Trommsdorff, V.: Subduction of water into the mantle: history of an Alpine peridotite, Geology, 23, 459–462, 1995.
Sengör, A. M. C., Altmer, D., Cin, A., Ustaömer, T., and Hsü, K. J.: Origin and assembly of the

SED
3, 477–526, 2011

Tethyside orogenic collage at the expense of Gondwana Land, J. Geol. Soc. London, Special Publication, 37, 119–181, 1988.
Shervais, J. W.: Ti-V plots and the petrogenesis of modern and ophiolitic lavas, Earth Planet. Sc. Lett., 59, 101–118, 1982.
Shervais, J. W., Dennis, A. J., McGee, J. J., and Secor, D.: Deep in the Heart of Dixie: Pre-Alleghanian Eclogite and HP Granulite Metamorphism in the Carolina Terrane, South Carolina, USA, J. Metamorph. Geol., 21, 65–80, 2003.
Shojaat, B., Hassanipak, A. A., Mobasher, K., and Ghazi, A. M.: Petrology, geochemistry and tectonics of the Sabzevar ophiolite, North Central Iran, J. Asian Earth Sci., 21, 1053–1067, 2003.
Spear, F. S.: Metamorphic Phase Equilibria and Pressure-Temperature-Time Paths, Mineralogical Society of America, Washington, DC, 1993.
Spear, F. S. and Kohn, M. J.: Trace element zoning in garnet as a monitor of crustal melting, Geology, 24, 1099–1102, 1996.
Spear, F. S. and Selverstone, J.: Quantitative P-T paths from zoned minerals: theory and tectonic applications, Contrib. Mineral. Petr., 83, 348–357, 1983.
Spray, J. G.: Possible causes and consequences of upper mantle decoupling and ophiolite displacement, in: Ophiolites and Oceanic Lithosphere, edited by: Gass, I. G., Lippard, S. J., and Shelton, A. W., J. Geol. Soc. London, UK, Special Publication, 13, 255–268, 1984.
Stampfli, G. M. and Borel, G. D.: A plate tectonic model for the Paleozoic and Mesozoic constrained by dynamic plate boundaries and restored synthetic oceanic isochrons, Earth Planet. Sc. Lett., 196, 17–33, 2002.
Stern, R. J.: Subduction Zones, Rev. Geophys., 40(4), 1012, doi:10.1029/2001RG000108, 2002.
Stöcklin, J.: Possible ancient continental margins in Iran, in: The geology of continent margins, edited by: Burke, C. A. and Darke, C. L., Springer, New York, 873–887, 1974.
Sun, S. S. and McDonough, W. F.: Chemical and isotopic systematics of oceanic basalts: implications for mantle composition and processes, in: Magmatism in Ocean Basins, edited by: Saunders, A. D. and Norry, M. J., J. Geol. Soc. London, Special Publication, 42, 312–345, 1989.
Sun, W. D., Bennett, V. C., Eggins, S. M., Arculus, R. J., and Perfit, M. R.: Rhenium systematics in submarine MORB and back-arc basin glasses: laser ablation ICPMS results, Chem. Geol., 196, 259–281, 2003.

SED
3, 477–526, 2011

Takin, M.: Iranian geology and continental drift in the Middle East, Nature, 235, 147–150, 1972.
Thorkelson, D. J. and Britsprecher, K.: Partial melting of slab window margins: genesis of adakitic and non-adakitic magmas, Lithos, 79, 25–41, 2005.
Thost, D. E., Hensen, B. J., and Motoyoshi, Y.: Two-stage decompression in garnet-bearing mafic granulits from Sostrene Island, Prydz Bay, East Antarctica, J. Metamorph. Geol., 9, 245–256, 1991.
Tirrul, R., Bell, I. R., Griffis, R. J., and Camp, V. E.: The Sistan Suture Zone of eastern Iran, Geol. Soc. Am. Bull., 94, 134–150, 1983.
Tomkins, H. S., Powell, R., and Ellis, D. J.: The pressure dependence of the zirconium-in-rutile thermometer, J. Metamorph. Geol., 25, 703–713, 2007.
Troitzsch, U. and Ellis, D. J.: Thermodynamic properties and stability of AlF-bearing titanite $CaTiOSiO_4$–$CaAlFSiO_4$, Contrib. Mineral. Petr., 142, 543–563, 2002.
Tropper, P., Manning, C. E., and Essene, E. J.: The substitution of Al and F in titanite at high pressure and temperature: Experimental constraints on phase relations and solid solution properties, J. Petrol., 43, 1787–1814, 2002.
Vielzeuf, D. and Schmidt, M. W.: Melting reactions in hydrous systems revisited: applications to metapelites, metagreywackes and metabasalts, Contrib. Mineral. Petr., 141, 251–267, 2001.
von Huene, R. and Scholl, D. W.: Observations at convergent margins concerning sediment subduction, subduction erosion, and the growth of continental crust, Rev. Geophys., 29, 279–316, 1991.
Wakabayashi, J. and Dilek, Y.: Spatial and temporal relationships between ophiolites and their metamorphic soles: a test of models of forearc ophiolite genesis, in: Ophiolites and Oceanic Crust: New Insight from Field Studies and the Ocean Drilling Program, edited by: Dilek, Y., Moores, E. M., Elthon, D., and Nicolas, A., Boulder Colorado, Geol S. Am. S., 349, 53–64, 2000.
Watson, E. B., Wark, D. A., and Thomas, J. B.: Crystallisation thermometers for zircon and rutile, Contrib. Mineral. Petr., 151, 413–433, 2006.
Whitney, D. L. and Evans, B. W.: Abbreviations for names of rock-forming minerals, Am. Mineral., 95, 185–187, 2010.
Willard, R. A. and Adams, M. G.: Newly discovered eclogite in the southern Appalachian orogen, Earth Planet. Sc. Lett., 123, 61–70, 1994.
Wilson, J. T.: Did the Atlantic colse and then re-open?, Nature, 211, 676–681, 1966.
Winchester, J. A. and Floyd, P. A.: Geochemical magma type discrimination: application to

SED
3, 477–526, 2011

altered and metamorphosed igneous rocks, Earth Planet. Sc. Lett., 28, 459–469, 1976.
Zack, T., Moraes, R., and Kronz, A.: Temperature dependence of Zr in rutile: empirical calibration of a rutile thermometer, Contrib. Mineral. Petr., 148, 471–488, 2004a.
Zanchi, A., Berra, F., Mattei, M., Ghasemi, M., and Sabouri, J.: Inversion tectonics in Central Alborz, Iran, J. Struct. Geol., 28, 2023–2037, 2006.
Zhao, G., Cawood, P. A., Wilde, S. A., and Liangzhao, L.: High-pressure granulites (retrograded eclogites) from the Hengshan complex, North China Craton: petrology and tectonic implications, J. Petrol., 42(6), 1141–1170, 2001.

SED
3, 477–526, 2011

Table 1. Major and trace element composition for the Sabzevar granulite samples.

Sample	NG 360	NG 362	NG 421	SZ290	368C	SZ283	EG354D	272	NG351
Major elements (wt %)									
SiO_2	48.22	47.22	45.99	43.63	41.25	48.85	48.07	47.58	41.85
Al_2O_3	12.71	12.55	12.92	14.44	15.00	14.50	12.37	12.85	14.28
FeO_{TOT}	16.17	15.28	15.53	9.14	15.08	11.56	17.11	16.50	15.07
MnO	0.31	0.27	0.25	0.15	0.21	0.31	0.20	0.27	0.26
MgO	7.05	7.59	6.51	10.81	12.69	8.80	7.29	6.53	10.49
CaO	7.76	10.04	10.87	15.66	8.34	7.43	8.40	9.69	13.05
Na_2O	2.39	2.46	1.35	1.18	2.19	2.87	2.26	2.09	1.79
K_2O	0.68	0.58	0.87	0.19	0.37	1.08	0.68	0.73	0.30
TiO_2	2.69	2.40	3.04	0.66	1.80	1.17	2.78	2.65	1.79
P_2O_5	0.27	0.26	0.28	0.07	0.11	0.06	0.31	0.26	0.20
LOI	1.13	0.99	0.80	3.12	2.81	1.75	0.86	0.92	1.36
Total (wt %)	99.38	99.63	98.40	99.06	99.85	98.38	100.30	100.10	100.40
Trace elements (ppm)									
Sc	47	48	48	49	58	35	50	48	59
Be	2	2	3	1	< 1	< 1	< 1	< 1	< 1
V	506	480	529	224	382	260	511	507	374
Sr	61	87	74	42	73	91	59	95	68
Ba	26	17	52	12	20	107	13	37	9
Cr	60	160	120	500	830	760	840	570	830
Co	43	48	38	46	62	40	51	46	59
Ni	40	80	60	130	370	360	460	310	370
Cu	40	50	50	< 10	60	310	40	90	50
Zn	120	40	130	80	160	500	150	140	120
Ga	19	18	19	14	18	16	22	20	17
Ge	2	2	2	1	2	2	2	2	2
As	< 5	< 5	< 5	< 5	< 5	< 5	< 5	< 5	< 5
Rb	8	5	13	1	4	21	6	14	1
Y	57	48	61	18	35	26	58	56	39
Zr	189	127	192	32	97	85	239	200	101

SED
3, 477–526, 2011

Table 1. Continued.

Sample	NG 360	NG 362	NG 421	SZ290	368C	SZ283	EG354D	272	NG351
Trace elements (ppm)									
Nb	5.7	5.4	5.9	2.5	9.1	2.6	6.5	5.1	6.6
Mo	< 2	< 2	< 2	< 2	4	5	7	5	4
Ag	< 0.5	< 0.5	< 0.5	1	< 0.5	< 0.5	< 0.5	< 0.5	< 0.5
In	< 0.1	< 0.1	< 0.1	< 0.1	< 0.1	< 0.1	< 0.1	< 0.1	< 0.1
Sn	3	1	2	< 1	2	2	4	3	2
Sb	< 0.2	< 0.2	< 0.2	4.80	< 0.2	< 0.2	< 0.2	< 0.2	< 0.2
Cs	0.20	0.10	0.30	< 0.1	0.30	0.30	0.10	0.40	< 0.1
La	7.94	10.70	9.16	3.04	3.44	4.38	10.50	7.72	9.17
Ce	22.00	25.40	25.40	7.13	9.01	11.00	30.30	22.60	22.10
Pr	3.53	4.23	3.96	1.05	1.49	1.69	4.91	3.73	3.27
Nd	18.00	21.00	20.40	5.69	8.13	8.39	24.40	19.40	15.50
Sm	6.06	6.91	6.81	1.90	3.30	2.87	8.14	6.47	4.88
Eu	2.00	2.18	2.28	0.77	1.26	0.94	2.51	2.03	1.80
Gd	6.44	8.54	7.26	2.46	4.66	3.84	9.88	8.45	6.02
Tb	1.62	1.58	1.80	0.47	0.94	0.74	1.77	1.63	1.14
Dy	9.94	9.15	11.00	3.00	6.01	4.58	10.70	10.00	6.94
Ho	2.18	1.97	2.41	0.62	1.29	0.96	2.11	2.14	1.40
Er	6.04	5.47	6.80	1.81	3.90	2.83	5.88	6.22	4.05
Tm	0.99	0.86	1.11	0.26	0.61	0.44	0.86	0.95	0.62
Yb	5.91	5.47	6.73	1.56	4.14	2.85	5.39	6.17	3.98
Lu	0.87	0.78	0.97	0.22	0.70	0.45	0.85	1.00	0.63
Hf	4.70	3.40	5.00	0.90	2.00	1.70	4.70	4.20	1.90
Ta	0.48	0.39	0.50	0.15	0.59	0.18	0.44	0.38	0.46
W	0.60	< 0.5	< 0.5	< 0.5	3.70	1.50	1.40	0.60	1.10
Tl	< 0.05	< 0.05	0.08	< 0.05	0.07	0.13	< 0.05	0.12	< 0.05
Pb	< 5	< 5	< 5	6.00	< 5	< 5	< 5	< 5	< 5
Bi	< 0.1	< 0.1	< 0.1	< 0.1	< 0.1	< 0.1	< 0.1	< 0.1	< 0.1
Th	0.41	0.83	0.47	0.19	0.45	0.47	0.66	0.52	0.69
U	0.32	0.56	0.19	0.04	0.04	0.11	0.32	0.39	0.26
$(La/Sm)^*_N$	0.85	1	0.87	1.03	0.73	0.65	0.95	0.81	0.75

* Normalised values after CI chondrite values (Sun and McDonough, 1989).

SED
3, 477–526, 2011

Table 2a. Representative EMPA analyses of garnet.

Sample	NG353				EG354		SZ290		NG421	
Analysis	#48-c	#43-r	#36-c	#42-r	#24-c	#10-r	#6-c	#13-r	70	130
SiO_2	37.67	37.46	37.55	37.47	37.90	37.65	38.55	38.59	39.01	37.64
TiO_2	0.12	0.17	0.12	0.20	0.17	0.18	0.15	0.10	0.10	0.11
Al_2O_3	22.09	22.00	21.99	21.51	21.46	21.47	21.71	21.73	21.42	20.78
Cr_2O_3	0.03	bdl	0.01	0.01	0.02	bdl	0.08	0.02	bdl	bdl
Fe^2O_3	2.16	2.41	2.84	2.38	1.49	2.01	2.73	2.66	0.00	2.71
FeO	23.53	23.04	23.26	22.97	22.76	22.77	17.89	20.15	25.20	23.54
MnO	1.66	1.57	2.12	1.98	2.59	2.45	0.77	0.90	1.93	1.11
MgO	4.54	3.89	4.74	3.71	3.13	3.06	7.47	7.91	3.96	4.07
CaO	9.21	10.35	8.56	10.38	11.16	11.11	11.05	8.57	8.37	10.28
Na_2O	0.01	0.02	0.04	0.02	0.04	0.04	0.02	0.02	bdl	bdl
K_2O	bdl	0.01	bdl	bdl	0.01	0.02	bdl	bdl	bdl	bdl
Totals	100.81	100.68	100.95	100.40	100.58	100.55	100.14	#####	99.99	100.24
Oxygens	12	12	12	12	12	12	12	12	12	12
Si	2.92	2.91	2.91	2.93	2.96	2.95	2.94	2.94	3.05	2.95
Ti	0.01	0.01	0.01	0.01	0.01	0.01	0.01	0.01	0.01	0.01
Al	2.02	2.02	2.01	1.98	1.98	1.98	1.95	1.95	1.97	1.92
Cr	0.00	0.00	0.00	0.00	0.00	0.00	0.01	0.00	0.00	0.00
Fe^3	0.13	0.14	0.17	0.14	0.09	0.12	0.16	0.15	0.00	1.60
Fe^2	1.53	1.50	1.51	1.50	1.49	1.49	1.14	1.29	1.65	1.55
Mn	0.11	0.10	0.14	0.13	0.17	0.16	0.05	0.06	0.13	0.07
Mg	0.53	0.45	0.55	0.43	0.36	0.36	0.85	0.90	0.46	0.48
Ca	0.77	0.86	0.71	0.87	0.93	0.93	0.90	0.70	0.70	0.86
Na	0.00	0.00	0.01	0.00	0.01	0.01	0.00	0.00	0.00	0.00
K	0.00	0.00	0.00	0.00	0.00	0.00	0.00	0.00	0.00	0.00
Sum	8.00	8.00	8.00	8.00	8.00	8.00	8.00	8.00	8.00	8.00

Mineral formula and ferric iron recalculation obtained through the software AX2000, enclosed in the THERMOCALC Package.
bdl – below detection limit; c – core; r – rim.

SED
3, 477–526, 2011

Table 2b. Representative EMPA analyses of Clinopyroxene.

Sample	NG353					EG354		SZ290		NG421		
Analysis	#68-m	#70-m	#28-m	#50-m	#28-m	#29-i	#38-m	#22-i	#19-c	50	136	131
SiO_2	49.73	48.18	49.61	50.34	49.61	50.70	49.82	49.05	49.07	50.66	50.90	49.30
TiO_2	0.40	0.61	0.40	0.25	0.40	0.30	0.49	0.30	0.32	0.60	0.32	0.55
Al_2O_3	4.04	5.18	4.11	2.82	4.11	2.87	3.78	6.62	7.00	2.96	2.26	5.00
Cr_2O_3	bdl	bdl	bdl	bdl	bdl	0.04	0.04	0.05	0.04	bdl	bdl	bdl
Fe^2O_3	2.59	4.38	2.81	2.41	2.83	1.56	1.65	3.23	3.41	0.79	2.30	2.18
FeO	9.69	8.09	9.79	9.79	9.77	9.96	9.74	4.70	4.61	12.49	10.94	10.78
MnO	0.36	0.31	0.40	0.37	0.40	0.20	0.15	0.21	0.21	0.31	0.18	0.24
MgO	10.66	10.26	10.29	11.17	10.29	11.51	10.87	13.00	12.74	10.99	11.50	10.38
CaO	21.37	21.99	21.25	21.22	21.25	21.57	21.44	21.36	20.94	20.83	21.35	21.15
Na_2O	0.73	0.71	0.84	0.68	0.84	0.55	0.70	0.73	0.98	0.44	0.47	0.59
K_2O	0.00	0.00	0.01	0.00	0.01	0.01	0.01	0.03	0.02	bdl	bdl	0.03
Totals	99.31	99.27	99.22	98.81	99.51	99.12	98.53	98.95	99.00	100.07	100.22	100.20
Oxygens	6	6	6	6	6	6	6	6	6	6	6	6
Si	1.89	1.83	1.89	1.92	1.89	1.93	1.90	1.83	1.83	1.92	1.93	1.86
Ti	0.01	0.02	0.01	0.01	0.01	0.01	0.01	0.01	0.01	0.02	0.01	0.02
Al	0.18	0.23	0.18	0.13	0.18	0.13	0.17	0.29	0.31	0.13	0.10	0.22
Cr	0.00	0.00	0.00	0.00	0.00	0.00	0.00	0.00	0.00	0.00	0.00	0.00
Fe^3	0.07	0.13	0.08	0.07	0.08	0.05	0.05	0.09	0.10	0.02	0.66	0.06
Fe^2	0.31	0.26	0.31	0.31	0.31	0.32	0.31	0.15	0.14	0.40	0.35	0.34
Mn	0.01	0.01	0.01	0.01	0.01	0.01	0.01	0.01	0.01	0.01	0.01	0.01
Mg	0.60	0.58	0.58	0.64	0.58	0.65	0.62	0.72	0.71	0.62	0.65	0.59
Ca	0.87	0.90	0.87	0.87	0.87	0.88	0.88	0.85	0.84	0.85	0.87	0.86
Na	0.05	0.05	0.06	0.05	0.06	0.04	0.05	0.05	0.07	0.03	0.03	0.04
K	0.00	0.00	0.00	0.00	0.00	0.00	0.00	0.00	0.00	0.00	0.00	0.00
Sum	4.00	4.00	4.00	4.00	4.00	4.00	4.00	4.00	4.00	4.00	4.00	4.00

Mineral formula and ferric iron recalculation obtained through the software AX2000, enclosed in the THERMOCALC Package.
bdl – below detection limit; c – core; i – inclusion; m – matrix.

SED
3, 477–526, 2011

Table 2c. Representative EMPA analyses of Plagioclase.

Sample	NG353		EG354		NG421	
Analysis	Pl	Pl	Pl	Pl	Pl	Pl
SiO_2	55.73	54.92	56.40	67.75	63.08	66.72
TiO_2	0.05	0.01	0.01	0.01	bdl	bdl
Al_2O_3	29.30	29.64	28.89	21.13	23.37	20.63
Cr_2O_3	0.01	0.01	bdl	bdl	bdl	bdl
Fe^2O_3	bdl	bdl	bdl	bdl	1.08	0.15
MnO	0.04	bdl	bdl	bdl	bdl	bdl
MgO	0.01	bdl	0.01	0.01	0.02	bdl
CaO	10.13	9.91	9.46	0.93	1.99	1.60
Na_2O	5.60	5.76	6.34	11.23	8.18	10.91
K_2O	0.16	0.37	0.08	0.04	2.14	0.11
Totals	101.03	100.62	101.19	101.10	99.87	100.12
Oxygens	8	8	8	8	8	8
Si	2.47	2.45	2.50	2.93	2.50	2.92
Ti	0.00	0.00	0.00	0.00	0.00	0.00
Al	1.53	1.56	1.51	1.08	1.51	1.07
Cr	0.00	0.00	0.00	0.00	0.00	0.00
Fe^3	0.02	0.01	0.01	0.01	0.01	0.00
Mn	0.00	0.00	0.00	0.00	0.00	0.00
Mg	0.00	0.00	0.00	0.00	0.00	0.00
Ca	0.48	0.48	0.45	0.04	0.45	0.08
Na	0.48	0.50	0.55	0.94	0.55	0.93
K	0.01	0.02	0.01	0.00	0.01	0.01
Sum	5.00	5.02	5.02	5.00	5.02	5.01

bdl – below detection limit.

SED
3, 477–526, 2011

Table 2d. Representative EMPA of Amphibole.

Sample	NG353			NG421		EG354	SZ290
Analysis	#65-m	#47-m	#44-i	#37-m	#85-m	#32-m	#2-m
SiO2	41.18	44.27	41.88	43.04	43.27	42.62	40.80
TiO_2	2.13	1.37	1.38	1.78	1.82	2.09	1.21
Al_2O_3	12.67	11.67	11.62	11.88	12.08	12.08	14.68
Cr_2O_3	0.01	0.05	0.02	0.03	0.05	0.02	0.26
Fe^2O_3	2.16	1.22	2.21	2.59	2.96	2.43	2.92
FeO	15.35	16.84	16.10	14.64	15.19	14.28	11.42
MnO	0.28	0.21	0.14	0.17	0.25	0.18	0.11
MgO	9.25	8.97	8.89	9.96	9.57	10.14	11.36
CaO	11.50	11.07	10.96	11.15	10.93	11.15	11.38
Na_2O	1.77	2.09	1.90	1.70	1.86	1.98	2.81
K_2O	0.76	0.65	0.70	0.67	0.63	0.42	0.26
Totals	96.84	98.29	95.58	97.35	98.31	97.14	96.91
Oxygens	23	23	23	23	23	23	23
Si	6.24	6.59	6.43	6.43	6.42	6.37	6.07
Ti	0.24	0.15	0.16	0.20	0.20	0.24	0.14
Al	2.26	2.05	2.10	2.09	2.11	2.13	2.57
Cr	0.00	0.01	0.00	0.00	0.01	0.00	0.03
Fe^3	0.25	0.14	0.26	0.29	0.33	0.27	0.33
Fe^2	1.95	2.10	2.07	1.83	1.88	1.79	1.42
Mn	0.04	0.03	0.02	0.02	0.03	0.02	0.01
Mg	2.09	1.99	2.04	2.22	2.12	2.26	2.52
Ca	1.87	1.77	1.80	1.79	1.74	1.79	1.81
Na	0.52	0.60	0.57	0.49	0.54	0.57	0.81
K	0.15	0.12	0.14	0.13	0.12	0.08	0.05
Sum	15.68	15.58	15.67	15.59	15.60	15.61	15.87

m – matrix; i – inclusion.

SED
3, 477–526, 2011

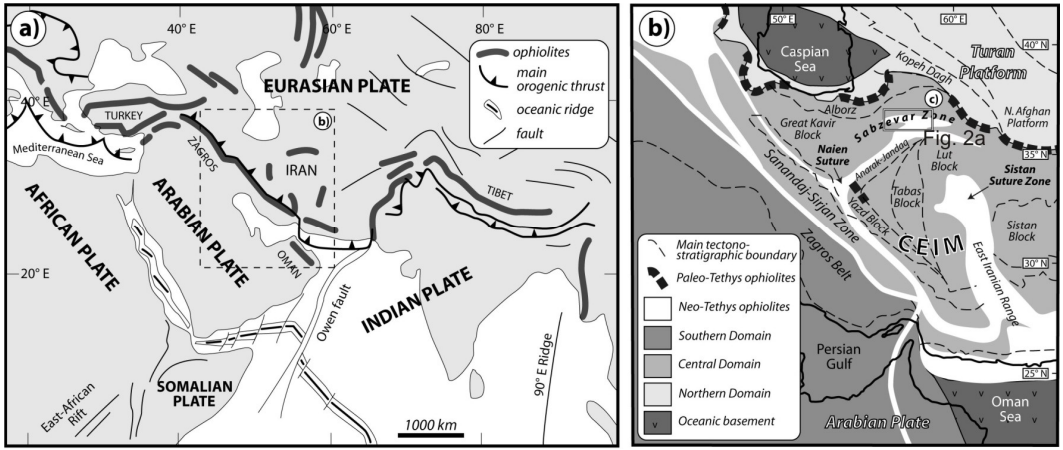

Fig. 1. **(a)** Distribution of the Tethyan ophiolitic suture zone along the Alpine-Himalayan convergence zone. **(b)** Simplified geological map showing the main tectonic domains in Iran, with the main (Neotethyan) ophiolitic belts (in white) indicated (modified after Shojaat et al., 2003; Bagheri and Stampfli, 2008). CEIM: Central East Iranian Microcontinent.

SED
3, 477–526, 2011

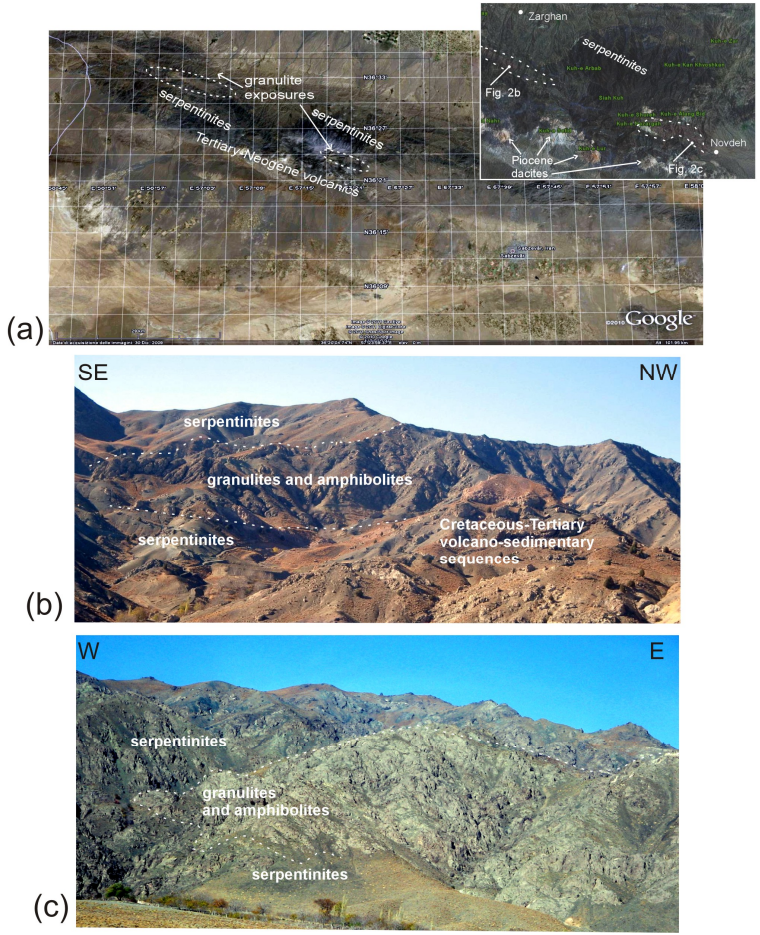

Fig. 2. **(a)** Satellite image of the Sabzevar Range and location of the granulite exposures (inset). (**b** and **c**) Field exposures and characteristics of the granulite/serpentinite contacts. The granulites occur as massive bodies enclosed within the serpentinite mass.

SED
3, 477–526, 2011

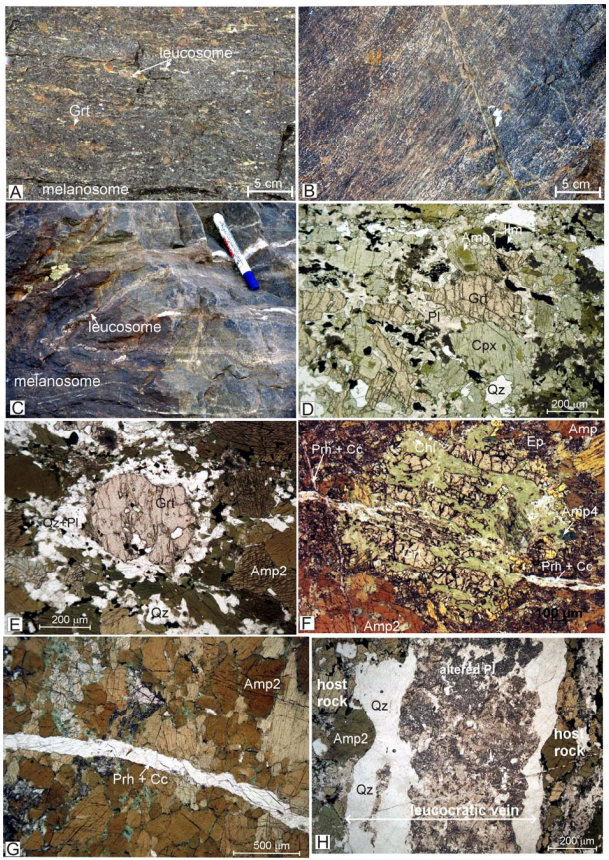

Fig. 3. **(a–c)** Granulite texture at the meso-scale. Note the presence of millimetric-to-centimetric leucocratic layers and patches that impart a stromatic texture to the rock. **(d–e)** Matrix assemblages at the thin section scale showing poikiloblastic garnet and clinopyroxene. Amphibole-plagioclase forms the main inclusion assemblage. Quartz-Plagioclase films surround garnet. **(f)** Porpyroclastic garnet surrounded by coronitic amphibole and late chlorite overgrowth. **(g)** Prehenite-calcite vein cutting across matrix amphibole. **(h)** Plagioclase alteration in leucosome.

SED
3, 477–526, 2011

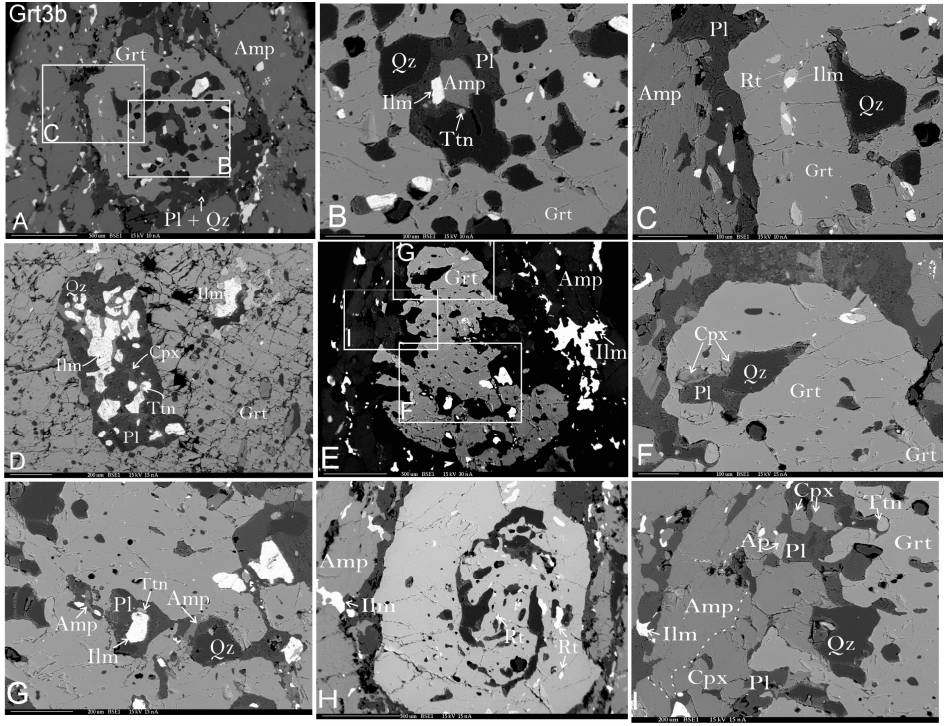

Fig. 4. Back scattered Electron images showing mineral and textural characteristics of the Sabzevar granulites (samples NG353 and NG421). **(a–c)** Poikiloblastic garnet with details on the core-rim distribution of the inclusion assemblages. The Ti-phases inclusions consist of ilmenite-titanite (Ilm_1/Ttn_1) at the garnet core **(b)** and of rutile that substitute ilmenite at the garnet rim **(c)**. **(d)** Garnet core hosting ilmenite pseudomorphs after titanite. The inclusion assemblages also consists of clinopriroxene and plagioclase. **(e)** Large porphyroblastic garnet with details on the core-rim inclusion assemblages: amphibole occurs at the garnet core **(f)**, whereas clinopyroxene at the garnet rim **(g)**. Note that composite ilmenite-titanite (Ilm_1-Ttn_1) assemblages occurs at the garnet core. **(h)** Rutile-bearing spiral trails of mineral inclusion in porphyroblastic garnet. Ilmenite occurs in the matrix assemblage (Ilm_2). **(i)** Poikyloblastic garnet and granular texture of the leucocratic quartz-plagioclase segregation. Titanite (Ttn_2) and ilmenite (Ilm_2) both occurs dispersed in the matrix assemblage.

SED
3, 477–526, 2011

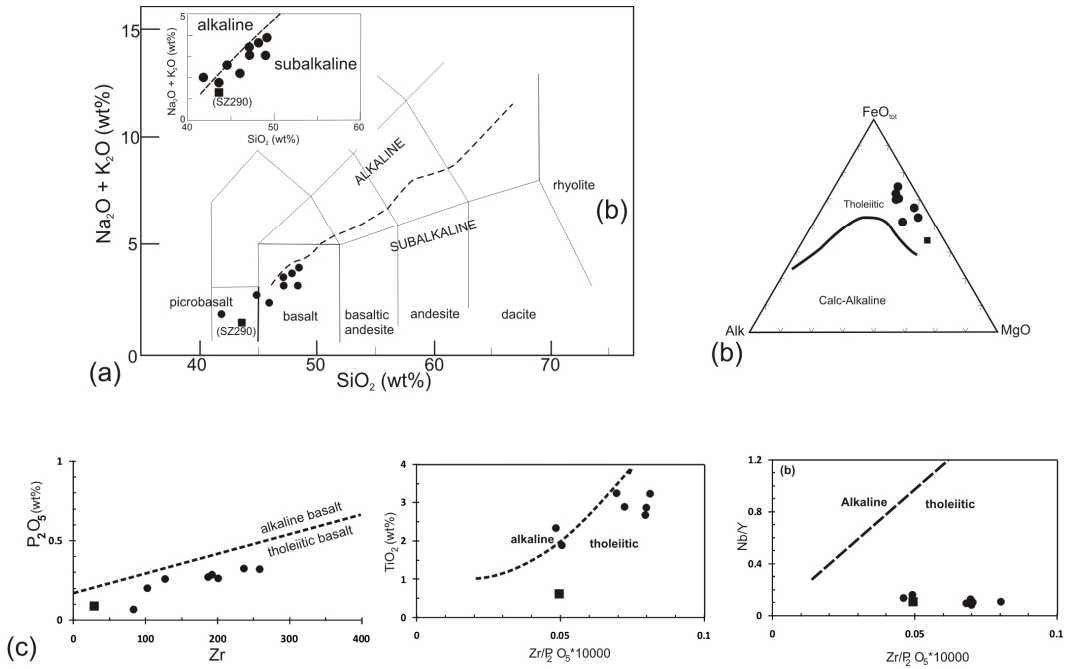

Fig. 5. Classification diagrams for the Sabzevar granulites. **(a)** Plot of total alkali vs. silica (Le Bas et al., 1992). The inset shows the alkaline/subalkaline fields after Kuno (1968); **(b)** AFM diagram after Irivine and Baragar (1971); **(c)** after Winchester and Floyd (1976). Key to symbols: square is sample SZ290.

SED
3, 477–526, 2011

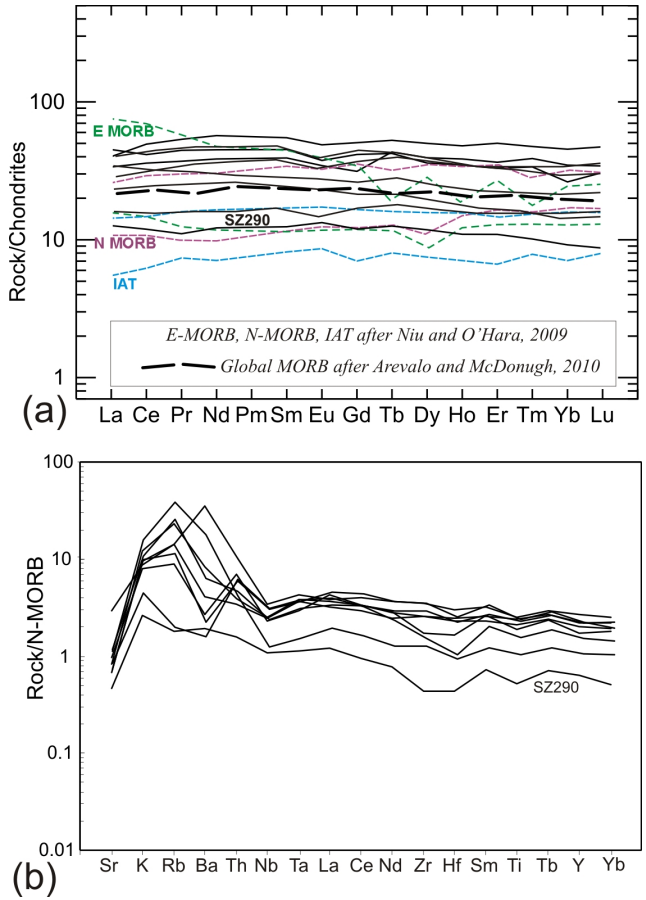

Fig. 6. Chondrite normalised REE patterns **(a)** and MORB-normalised trace element spiderdiagrams **(b)** for the Sabzevar granulites. Normalised values are after Sun and McDonough (1989).

SED
3, 477–526, 2011

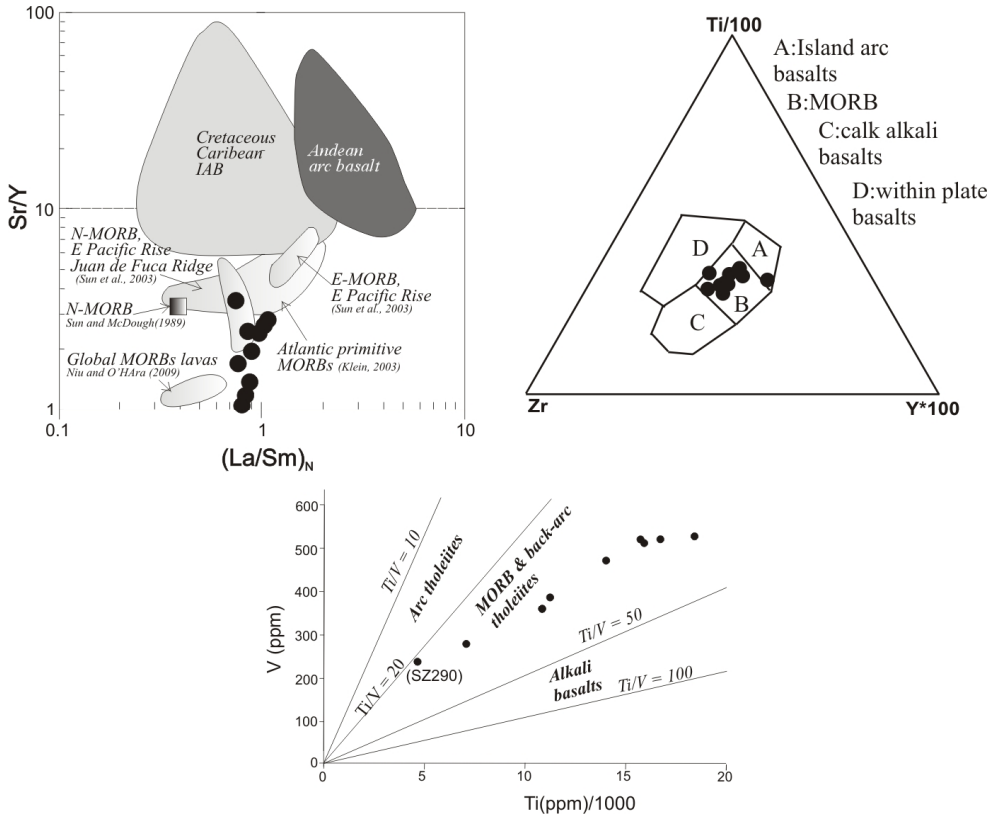

Fig. 7. Geotectonic discrimination diagrams for the Sabzevar granulites. **(a)** Sr/Y vs. $(La/Sm)_N$ diagram (after Berger et al., 2009 and references therein). **(b)** After Pearce and Cann (1973); **(c)** after Shervais (1982).

SED
3, 477–526, 2011

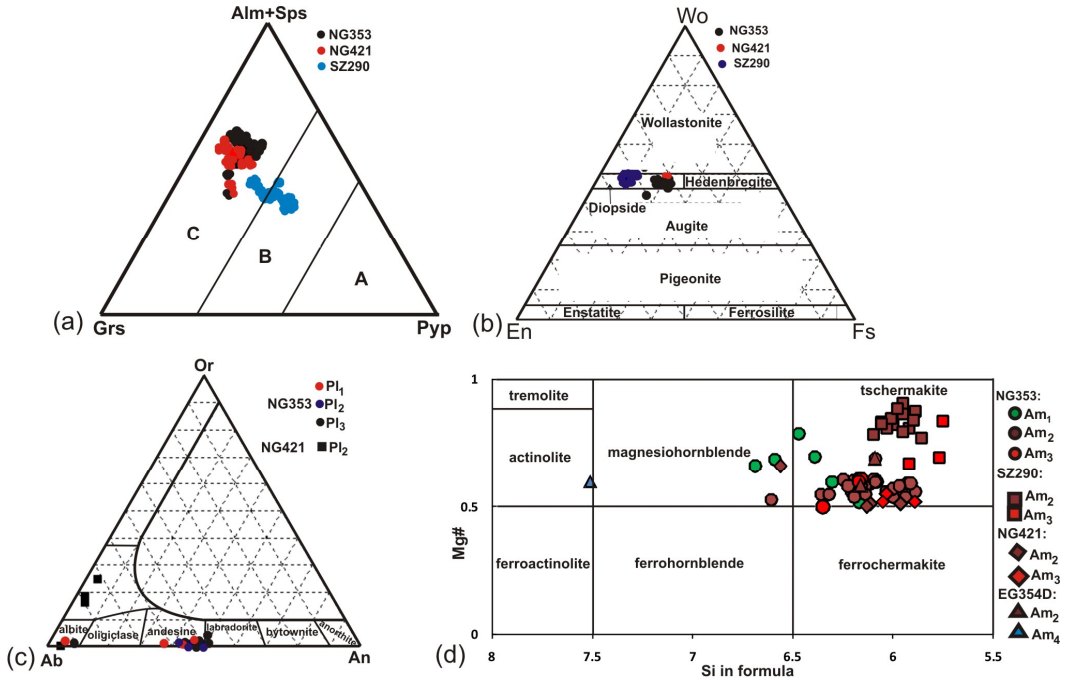

Fig. 8. Mineral classification diagrams. **(a)** garnet, after Coleman et al. (1965); **(b)** pyroxene and **(c)** feldspar, after Deer et al. (1991); **(d)** amphibole, after Leake et al. (2004).

SED
3, 477–526, 2011

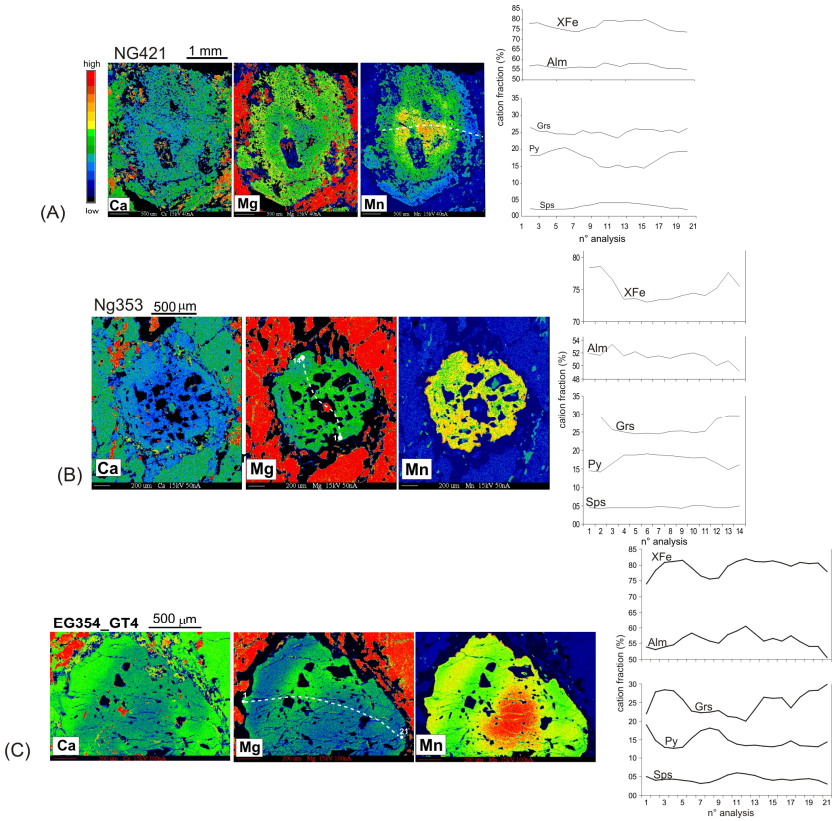

Fig. 9. Left: representative qualitative compositional cation map and quantitative cation profiles showing the variation in cation (Mg, Fe, Ca, Mn) distribution in garnets from the Sabzevar granulites Noteworthy features are the rimward increase in Ca (grossular) and Mn (spessartine, Sps) and decrease in Mg (pyrope), which are indicative of retrograde diffusion and resorbtion. Alm, almandine; Grs, grossular; Py, pyrope; Sps, spessartine. Right: garnet compositions as obtained through EMPA chemical profiles across the same garnet grains (dashed white line).

SED
3, 477–526, 2011

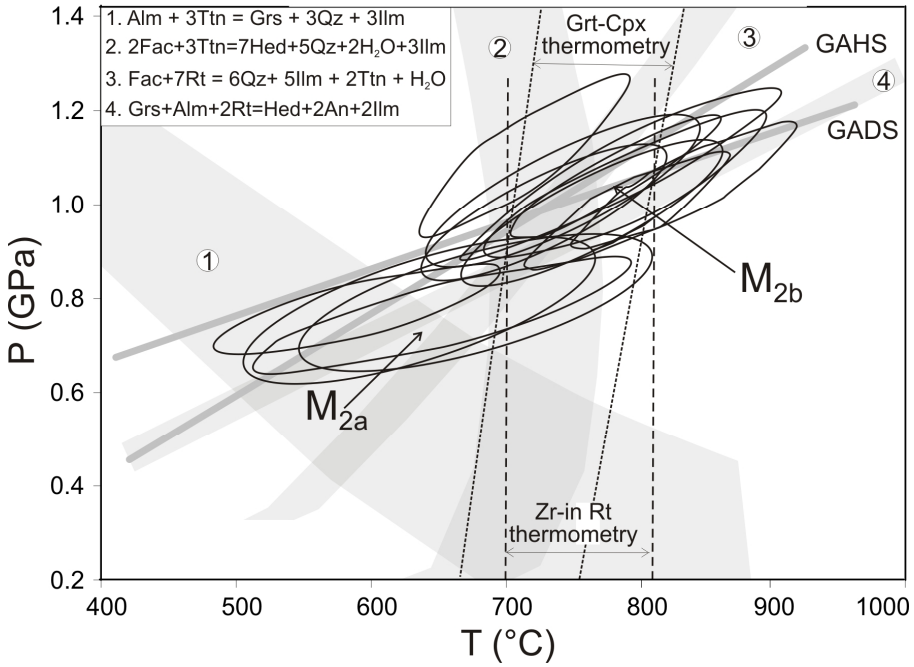

Fig. 10. Results from conventional thermobarometry, compared with those obtained from the THERMOCALC software in the average *P-T* calculation mode. The latter results are shown as best fit ellipses, with error quoted at 1σ level. The grey areas show the *P-T* fields calculated with the THERMOCALC software that pertain to the single reactions (numbered in the inset) that involve the Ti-bearing phases relevant for the main rock forming mineral assemblages (mineral abbreviations follow Whitney and Evans, 2010). See text for further details.

SED
3, 477–526, 2011

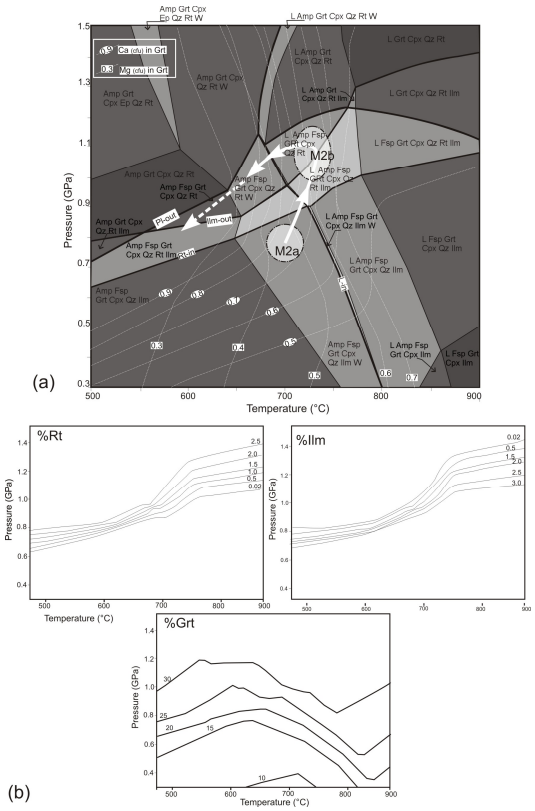

Fig. 11. **(a)** Representative *P-T* pseudosection calculated for the Sabzevar granulites in the system NCFMASHMnTO with a bulk composition (wt %) Na_2O 1.35, CaO 10.87, FeO 15.53, MgO 6.51, Al_2O_3 12.92, SIO_2 45.99, MnO, 0.25, H_2O 1.0, TiO_2 3.04, O_2 0.01 by using the Perple_X07 software. The dashed grey circles enclose the *P-T* spaces in which the M_1 and M_2 (metamorphic climax) assemblages are inferred to be located. The dashed white arrow indicates the *P-T* path followed by the Sabzevar granulites during their prograde and retrograde history. **(b)** Predicted modal distribution (% wt) of rutile, ilmenite (top) and garnet (bottom) in the modelled *P-T* field. Mineral abbreviations follow Whitney and Evans (2010) except for L, melt and W, H_2O.

SED
3, 477–526, 2011

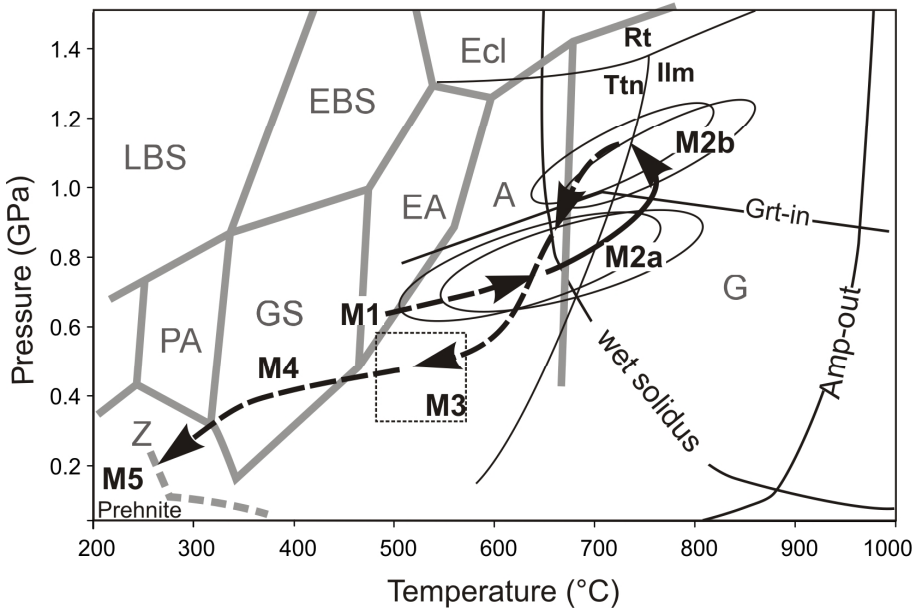

Fig. 12. Proposed synthetic *P-T* path for the Sabzevar granulites. Metamorphic facies boundaries are after Bucher and Frey (2002). The grid showing wet melting regimes for basaltic system with stability of the main index minerals indicated is after Vielzieuf and Schmidt (2001). Experimentally determined *P-T* field phase boundaries for Ti-phases (Ttn, Ilm, Rt) are after Liou et al. (1998). The prograde M_1-to-M_2 and the retrograde M_3-to-M_5 paths are only tentative. Key to symbols: A, amphibolite facies; EA, epidote amphibolite facies; EBS, epidote blueschist facies; Ecl, eclogite facies; G, granulite facies; GS, greenschist facies; LBS, lawsonite-blueschist facies; PA, pumpelliite-actinolite facies; Z, zeolite facies. Mineral Abreviations are after Whitney and Evans (2010).

SED
3, 477–526, 2011